Petroleum Science 22 (2025) 5097–5113

Contents lists available at ScienceDirect

Petroleum Science

journal homepage: www.keaipublishing.com/en/journals/petroleum-science

Original Paper

The heat-fluid-solid coupling erosion mechanism for the optimal spray distance and jet angle in high-pressure water jets

Mu-Kun Li [a], Cai-Yun Xiao [b,*], Xue Sun [c], Hong-Jian Ni [d], Yu-Kun Du [d]

[a] College of Safety and Environmental Engineering, Shandong University of Science and Technology, Qingdao, 266590, Shandong, China
[b] School of Resources and Safety Engineering, Chongqing University, Chongqing, 400044, China
[c] College of Energy and Mining Engineering, Shandong University of Science and Technology, Qingdao, 266590, Shandong, China
[d] School of Petroleum Engineering, China University of Petroleum (East China), Qingdao, 266580, Shandong, China

ARTICLE INFO

Article history:
Received 10 November 2024
Received in revised form
4 October 2025
Accepted 8 October 2025
Available online 10 October 2025

Edited by Jia-Jia Fei

Keywords:
High-pressure water jet
Erosion stress
Heat-fluid-solid coupling
Viscous dissipation
Temperature field
Pressure field

ABSTRACT

Focusing on the conversion of pressure energy and internal energy under viscous dissipation, a heat-fluid-solid coupling method is established to study the flow and stress fields of 100 MPa submerged water jets. Results indicate that pressure energy to internal energy conversion primarily occurs at three locations: the nozzle wall, the potential core edge, and the impact wall, with the most intense conversion occurring at the impact wall. The impact temperature of the jet can reach 200 °C, and the high-temperature region covers an area more than 4 times that of the high-pressure. Thermal stress can especially amplify erosion stress by more than 100% and expand the erosion area by more than 400%. Therefore, it serves as a dominant factor determining the optimal spray distance and jet angle in hard rock ($E \geq 40$ GPa). With increased spray distance or jet angle, impact pressure decreases, while the high-temperature zone moves toward the high-pressure region, thus increasing the overlap between the two regions. This extended overlap enhances the temperature-pressure coupling effect, consequently reducing the threshold pressure for jet-breaking rock. Therefore, the maximum erosion stress increases first and then decreases, and an optimal spray distance and jet angle exist. The optimal jet angle, defined by the maximum tensile stress, decreases with the dimensionless spray distance increase, ranging between 0° and 40°. This temperature-pressure coupling reduces rock-breaking threshold pressure by 15%–75% for elastic moduli of 40–80 GPa, with maximum erosion stress peaking at a dimensionless spray distance of 9 and jet angles of 15°–20°. When the overlap region decreases, the area affected by the temperature and pressure fields increases, leading to an increase in the rock-breaking area. It is important to note that reducing the rock-breaking threshold pressure and increasing the rock-breaking area are mutually exclusive objectives. It is necessary to optimize the design of the spray distance and jet angle according to the on-site rock-breaking requirements.

© 2025 The Authors. Publishing services by Elsevier B.V. on behalf of KeAi Communications Co. Ltd. This is an open access article under the CC BY-NC-ND license (http://creativecommons.org/licenses/by-nc-nd/4.0/).

1. Introduction

Water jet is an adaptable, non-contact erosion technique extensively applied in various scenarios such as well drilling and completion (Li et al., 2010; Wang et al., 2023), horizontal well fracturing (Chen et al., 2022; Li et al., 2012; Liao et al., 2020), coal mine permeability enhancement (Yang et al., 2022), tunnel excavation (Liu et al., 2023; Zhang et al., 2023), mining (Huang et al., 2022), incremental sheet forming (Miroir et al., 2022), composite material processing (Dahiya et al., 2022), superhard material machining (Xiao et al., 2020), descaling and derusting (Yar'Adua et al., 2021), and metal surface modification (Liu et al., 2020). Higher water jet pressure can enhance erosion effectiveness, but it also increases energy consumption, manufacturing and maintenance costs, and safety risks. Enhancing the erosion capacity of water jets without increasing pressure can resolve critical technological bottlenecks and align with the development of low-carbon technologies. Thermal damage is primarily influenced by the thermodynamic properties of materials rather than their

* Corresponding author.
E-mail address: xiaocy@cqu.edu.cn (C.-Y. Xiao).
Peer review under the responsibility of China University of Petroleum (Beijing).

https://doi.org/10.1016/j.petsci.2025.10.001
1995-8226/© 2025 The Authors. Publishing services by Elsevier B.V. on behalf of KeAi Communications Co. Ltd. This is an open access article under the CC BY-NC-ND license (http://creativecommons.org/licenses/by-nc-nd/4.0/).

mechanical properties, which means low reliance on jet pressure. Introducing thermal shocks in the jet through the thermo-mechanical coupling actions of jet pressure and temperature can significantly boost erosion capabilities, exemplified by technologies like liquid nitrogen jets (Huang et al., 2019), high-temperature steam jets (Beentjes et al., 2018; Hu et al., 2019), and supercritical CO_2 (SC-CO_2) jets (Cai et al., 2022; Li et al., 2021; Shen et al., 2023; Wang et al., 2015). Compared to these thermomechanical coupling jet erosion technologies, high-pressure water jets pose lower equipment requirements and accessibility barriers. Exploring how to increase the erosion capacity of water jets through thermal stress is currently at the cutting edge of scientific research and presents significant challenges.

The current theory of high-pressure water jet erosion struggles to account for the optimal spray distances and jet angles. Theoretical studies have shown that as the submerged jet's spray distance or jet angle (between the nozzle axis and the wall perpendicular) increases, the impact pressure diminishes (Shen and Sun, 1988), negating the existence of an optimal spray distance or jet angle. However, experimental evidence suggests that the optimal spray distance for submerged water jets generally exceeds the potential core of jets and tends to increase with jet pressure (Srivastava et al., 2021). Unlike the optimal spray distance, the optimal jet angles for water jets generally range between 5° and 20° and are barely unaffected by jet pressure (Čuha and Hatala, 2022; Kobayashi et al., 1987; Tian et al., 2012; Zhao et al., 2017). For example, the residual compressive stress and the plastic deformation layer of the aluminum alloy at jet angle 20° are the maximum (Zhang et al., 2022). Some experiments have not observed the optimal jet angles or distances; notably, aluminum alloy with a high thermal expansion coefficient demonstrates optimal spray distances, whereas steel with a lower thermal expansion coefficient does not (Kobayashi et al., 1987; Li et al., 2017a). The prevalent explanation is that erosion volume is determined by the erosion width and depth, and with the increase of spray distance, erosion width increases, and erosion depth decreases; thus, an optimal spray distance exists (Ozcelik et al., 2012; Oh and Cho, 2014). The optimal jet erosion angle explanations are the jet's reflection, duration of action, and the ploughing effect (Čuha and Hatala, 2022); hence, an optimal angle exists. Nonetheless, explanations for the optimal spray distance and jet angle remain vague, lacking quantitative data on the jet and stress fields.

When two adjacent layers of fluid move relative to each other, the high-speed shear flow, under the action of viscous stress, generates a significant amount of heat energy, resulting in a rapid rise in fluid temperature, known as viscous dissipation. Due to the high velocity of the high-pressure water jet, a velocity turn of about 90° is produced when the jet reaches the solid wall, resulting in a large velocity gradient and viscous dissipation near the jet center. *Br* (Brinkman number) is the heat-generated ratio from viscous dissipation to heat conduction. When *Br* is greater than 1, the viscous dissipation effect of the fluid must be considered. It is calculated that *Br* varies from 5 to 20 when the jet pressure ranges from 50 to 400 MPa, indicating that the viscous dissipation in a high-pressure water jet cannot be ignored. For a long time, water jets have been considered as low-heat or no-heat erosion technology, and the viscous dissipation and temperature distribution under high-pressure water jets have rarely been studied. Research on viscous dissipation and thermal deformation focuses on the hydraulic slide and throttle valves. Current research (Chen et al., 2020, 2021; Deng et al., 2009) shows that the valve wall temperature increases with the increase of throttle pressure difference and fluid viscosity, and the viscous dissipation heat generation effect increases with the growth of surface roughness. The maximum temperature rise can reach about 10 °C under the throttle pressure difference of 25 MPa pure water, and the valve body wall impacted by the jet of the throttle notch is a high-temperature area. The heat generated by viscous dissipation will cause the thermal deformation of the valve, resulting in the stagnation of the slide valve or the throttle valve. The valve body's thermal conductivity and thermal expansion coefficient have a more significant impact. The temperature of the valve body ranges from high to low in the order of stainless steel > structural steel > aluminum alloy. Still, the thermal expansion deformation ranges from high to low in the order of aluminum alloy > stainless steel > structural steel. The above thermal expansion results also correspond to Kobayashi's classic experiment (Kobayashi et al., 1987). Under the same conditions, the optimal spray distance of aluminum alloy is 180, but the optimal value does not exist for steel with a relatively low coefficient of thermal expansion, indicating that the thermal stress under viscous dissipation is an important influencing factor.

Existing high-pressure water jet erosion theories can be mainly divided into static elastic breakage, water wedge tensile breakage, dense core splitting breakage, stress wave breakage, cavitation erosion breakage, and damage theories (Ni and Wang, 2004; Zhang et al., 2022). However, the mechanism of heat-fluid-solid coupling erosion under viscous dissipation is still unclear, which cannot effectively guide the design of water jet tools and construction parameters. Therefore, combined with previous studies on jet energy conversion and thermal stress (Li et al., 2017b, 2020, 2021), this paper focuses on the temperature and pressure fields within submerged high-pressure water jets and their heat-fluid-solid coupling erosion mechanisms. A computational model for flow fields and erosion stresses is developed to examine how these variables change with spray distance and jet angle, providing a novel theoretical foundation for advancing high-pressure water jet erosion technology. This study also offers new insights and methodologies for understanding the erosion damage mechanisms in high-speed flows like drilling fluids and crude oil through pipelines and valves.

2. Computational model

2.1. Simulation assumptions

The permeability of the rock is negligible in the simulation due to the small impact of seepage on the rock-breaking by jet. The influence of rock deformation under the flow field is negligible because the rock deformation is less than the surface roughness of most rocks at the jet pressure difference of 100 MPa. The rock is assumed as a homogeneous medium because the different thermal expansion coefficients and temperature gradient are the main reasons for rock-breaking (Wang et al., 2019; Yu et al., 2023), but rock heterogeneity may exaggerate the temperature stress. The static elastic failure theory is adopted, i.e., the rock mainly undergoes tensile failure and shear failure under the jet, so static stress under the jet field is used as a criterion for evaluating rock failure.

2.2. Physical model, boundary conditions, and mesh configuration

A comprehensive full-scale physical model incorporating the nozzle, fluid, and solid domains is developed. The nozzle features a diameter (ϕ_n) of 1 mm, with the spray distance (D_{st}) ranging from 4 to 16 mm and the jet angle (θ) adjustable from 0 to 40°. The rock has a diameter of 100 mm and a thickness of 40 mm, with additional dimensions detailed in Fig. 1. Boundary conditions are assigned as pressure inlets and outlets at the nozzle and fluid boundaries, respectively, with a conjugate heat transfer condition

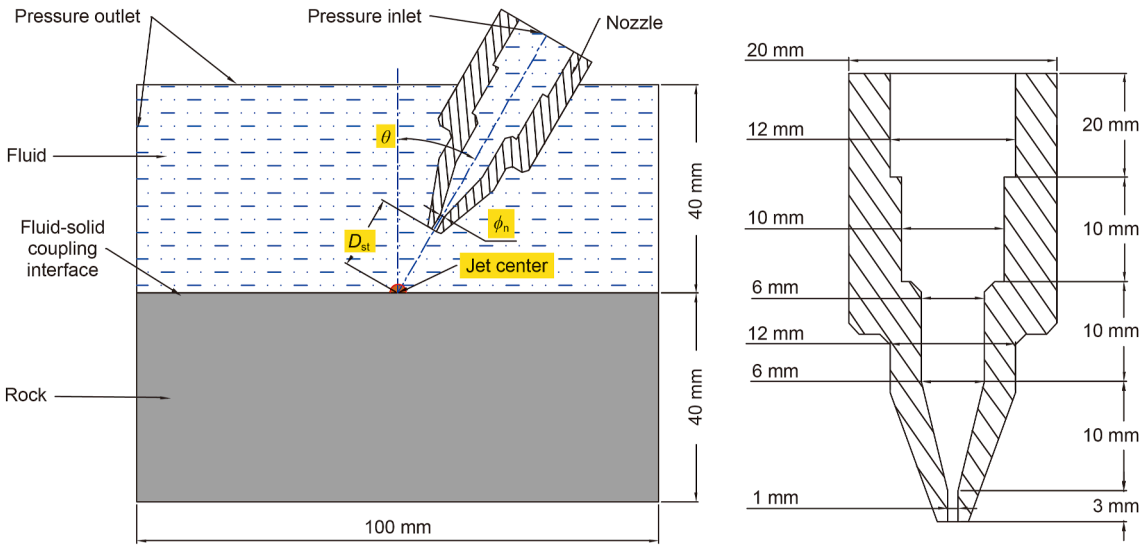

Fig. 1. Physical model and boundary conditions.

applied at the fluid-solid interface. For enhanced computational analysis, the nozzle radius is denoted as R_n, and the radial distance from a point on the rock surface to the jet's center is defined as D_{ra}, with D_{ra}/R_n representing the dimensionless radius and D_{st}/ϕ_n the dimensionless spray distance. The inlet pressure and outlet pressure are set to 100 and 1 MPa, respectively.

The meshing primarily employs hexahedral elements, achieving an average mesh quality of 0.99 (optimal quality is 1). To better capture temperature, velocity, and pressure fluctuations, the high-speed jet area, nozzle, jet core, and rock surface are subject to localized mesh refinement. The variation of impact pressure and impact temperature with the local mesh refinement size of 0.16 to 0.02 mm is conducted. The jet impact pressure and impact temperature show no difference when the refinement size is below 0.04 mm, proving that the mesh size no longer affects the calculation accuracy. Considering the computational efficiency, a local refinement size of 0.04 mm was finally adopted. In the jet core, mesh sizes are maintained at 0.04 mm, while the first boundary layer on the nozzle wall and rock surface is kept below 0.004 mm in thickness. The mesh configuration is depicted in Fig. 2.

2.3. Turbulence modeling and fluid property equations

The shear stress transport (SST) *k-w* turbulence model is utilized, combining the strengths of the *k-ε* and *k-w* models. This model excels in handling rotating flows and near-wall behaviors, effectively managing the transport of turbulent shear stresses within boundary layers influenced by adverse pressure gradients (Nieto et al., 2015; Hu et al., 2016).

Fluid properties are characterized using equations recommended by the National Institute of Standards and Technology (NIST), which reliably quantify and describe water's density, specific heat, viscosity, and thermal conductivity with temperature and pressure (Kestin et al., 1984; Wagner and Pruβ, 2002).

2.4. Constitutive and physical properties of the rock and heat conduction equations

Stress analysis is conducted in the static structural in ANSYS, correlating rock stress and strain as follows:

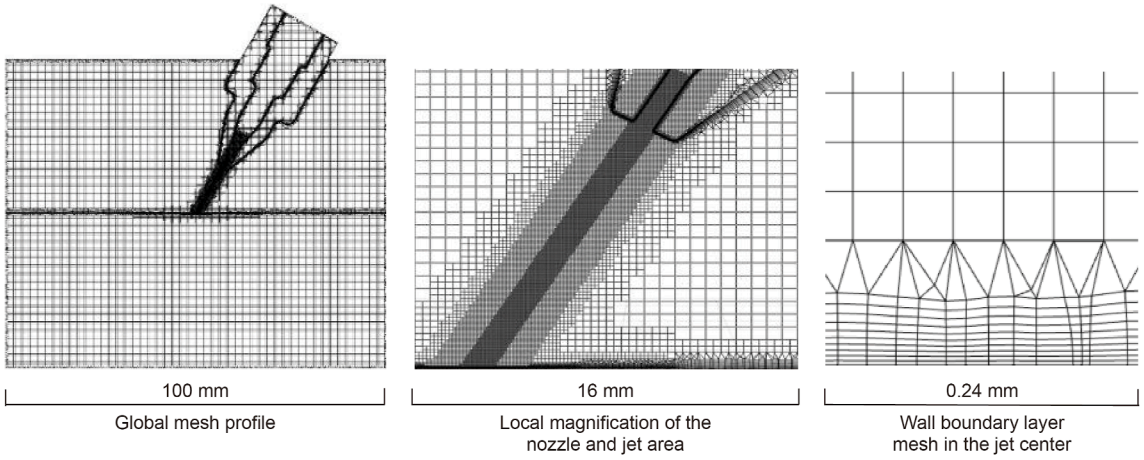

Fig. 2. Mesh configuration.

$$\varepsilon_{ii} = \alpha(T - T_0) + \frac{\sigma_{ii}}{E} - \frac{\upsilon\sigma_{jj}}{E} - \frac{\upsilon\sigma_{ll}}{E} \quad (1)$$

where ε_{ii} is the strain in direction i; α is the thermal expansion coefficient; T_0 and T are the initial and changed temperatures, respectively; σ_{ii}, σ_{jj} and σ_{ll} are the stress tensor in three directions on the coordinate; E is the Modulus of elasticity; and υ is Poisson's ratio.

The heat conduction equation employed is:

$$\rho C\frac{\partial T}{\partial t} = \frac{\partial}{\partial x}\left(\lambda\frac{\partial T}{\partial x}\right) + \frac{\partial}{\partial y}\left(\lambda\frac{\partial T}{\partial y}\right) + \frac{\partial}{\partial z}\left(\lambda\frac{\partial T}{\partial z}\right) + q_v \quad (2)$$

where ρ is the density, C is the heat capacity, λ is the thermal conductivity, and q_v is the heat generation rate.

Investigations into granite's mechanical and thermodynamic characteristics have helped define the simulation parameters for the rock's mechanical strength, thermodynamics, and surface roughness (K_s), detailed in Table 1.

2.5. Solution steps

There are mainly three steps.

(1) With the coupled heat transfer between the fluid and the rock disregarded, the boundary conditions are set with an inlet pressure of 100 MPa at the nozzle and an outlet pressure of 1 MPa in the fluid domain, allowing for the calculation of the steady-state impact temperature field and pressure field.
(2) The coupled heat transfer between the fluid and rock is incorporated, starting calculations at time zero from the flow field determined in step (1). This approach assesses the rock surface pressure and internal temperature fields within the rock core at the jet time (t_j) of 0.001 s.
(3) With the pressure and temperature fields from step (2) serving as initial conditions, a zero displacement constraint is imposed on the rock's base, and 1 MPa confining pressure is imposed on the rock's side wall. This setup is utilized to compute the tensile and shear stresses on the rock surface at time t_j.

3. Validation of simulation methods

Compared with heterogeneous materials like rocks, aluminum's mechanical and thermodynamic properties are more stable. There are detailed reference data, and the experimental results are more accurate and reliable. Therefore, we chose the experiment of water jet erosion of aluminum as the basis for verification of the calculation model. Kobayashi et al. performed experiments on the erosion of different metals by a water jet under a pressure of 50 MPa (Kobayashi et al., 1987; Li et al., 2017a), showing that when the central pressure loss ($p_{dr,\ exp}$) reached 0.275, there was a peak in the erosion mass of aluminum (*EW*) (Fig. 3). Considering the influence of the pressure measuring port on the jet's central pressure, we conducted a simulation with the aluminum alloy's mechanical and thermodynamic parameters shown in Table 2. We

Table 1
Mechanical and thermodynamic parameters of the rock.

ρ, kg/m^3	C, J/kg·K	λ, W/m·K	υ	E, GPa	α, K^{-1}	K_s, 10^{-6} m
2640	827	2.5	0.19	40	8.3×10^{-6}	50

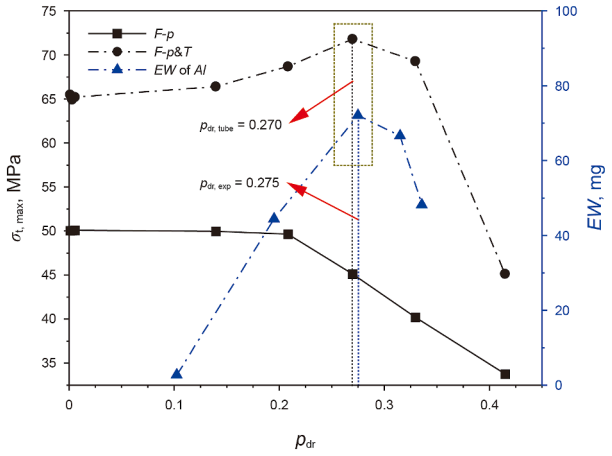

Fig. 3. Variation in maximum tensile stress and erosion mass with central pressure loss ratio.

Table 2
Mechanical and thermodynamic parameters of aluminum alloy.

ρ, kg/m^3	C, J/kg·K	λ, W/m·K	υ	E, GPa	α, K^{-1}	K_s, 10^{-6} m
2700	880	237	0.3	70	23×10^{-6}	10

defined p_{av1} and T_{av1} to represent the average central pressure and temperature near the jet center ($D_{ra}/R_n \leq 1$), respectively, and $p_{dr,\ tube}$ for the central pressure (p_{av1}) loss ratio with spray distance. The simulation findings indicated that the maximum tensile stress ($\sigma_{t,\ max}$) in the pressure field (*F-p*) did not peak with increasing central pressure loss ratio ($p_{dr,\ tube}$), yet under the temperature-pressure coupling field (*F-p&T*), the tensile stress peaked at a central pressure loss ratio of 0.27 (Fig. 3). The reasons can be explained well with the temperature contour in Fig. 4. Although the increasing central pressure loss with spray distance leads to a lower erosion tensile stress, the increasing central temperature magnifies the stress more quickly ($p_{dr,\ tube} < 0.27$). The peak in aluminum erosion mass and maximum tensile stress near a central pressure loss of 0.27 highlights that thermal stress is pivotal in determining the optimal erosion distance for water jets, affirming

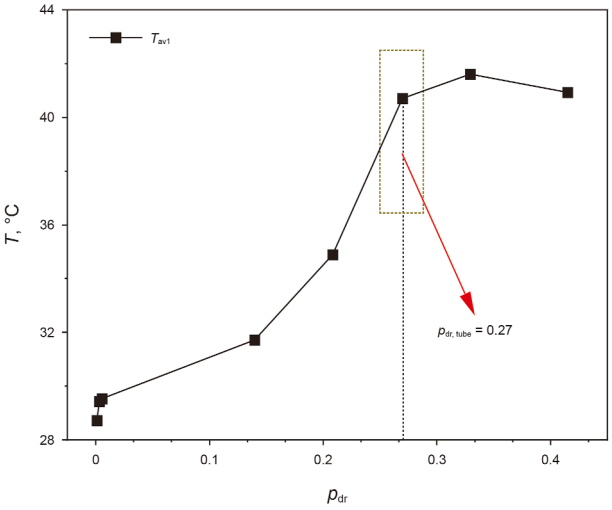

Fig. 4. Variation in central temperature (T_{av1}) with central pressure loss ratio ($p_{dr,\ tube}$).

the efficacy of the computational model and methodology developed in this study. There is a 0.5 difference between the central pressure loss ratio corresponding to the maximum erosion amount in the experiment and the central loss ratio corresponding to the maximum stress in the simulation. There are two most likely reasons: one is that there is an error in the pressure test, and the other is that the experimental conditions of the non-submerged jet are inconsistent with the simulated conditions of the submerged jet.

4. Variation in jet temperature and pressure fields

4.1. Transformation of the pressure field, velocity field, and temperature field in the jet

Fig. 5 shows the flow field variation in (a) pressure field, (b) velocity field, and (c) temperature field at a spray distance of 4 and jet angle of 30°. By comparing Fig. 5(a) and (b), we can see that the static pressure energy transforms into dynamic pressure energy through the nozzle. After the high-velocity jet impacts the wall, the dynamic pressure energy is transformed into static pressure energy. During the jet process, a large velocity gradient appears in the inner wall of the nozzle, the potential core (red part in Fig. 5(b)), and the area near the impact wall; that is, a high shear rate. Compared with Fig. 5(b) and (c), we can see that the inner wall of the nozzle, the potential core, and the area near the impact wall all have a temperature rise phenomenon. The temperature increases the most near the jet center ($\Delta T_{max} = 148$ °C), followed by the inner wall of the nozzle ($\Delta T_{max} = 24$ °C), and the temperature near the potential core increases the least ($\Delta T_{max} = 6$ °C), indicating that the damaging effect of thermal stress on the rock is more significant than that of the nozzle. From the perspective of the jet process, the jet fluid has undergone three viscous dissipative heating processes: nozzle wall, potential core, and impact wall. Both the high-pressure zone and high-shear rate appear near the jet center, so the maximum temperature appears near the jet center. The maximum temperature occurs in the viscous bottom layer with a high shear rate and low velocity within 1 μm near the impact wall, accounting for the accumulation of a large amount of heat under the impact of the high-velocity jet. The highest temperature occurs near a dimensionless radius of 2, which is also the edge of the high-pressure area and the place with relatively high flow velocity near the wall. The above results indicate that the conversion rate of static pressure energy to kinetic energy is the highest at this position. The greater kinetic energy is then converted into more internal energy at a higher shear rate in the fluid boundary layer. Therefore, the temperature rise amplitude is the greatest.

4.2. Variation in impact pressure and temperature with spray distance

Figs. 6 and 7 illustrate the contours of pressure and temperature on the rock surface at spray distances of 4, 8, and 10, respectively. In contrast, Fig. 8 depicts the curves of (a) impact pressure and (b) impact temperature distribution across spray distances of 4–14. By comparing Figs. 6–8, we can see that the maximum pressure occurs at the jet center and diminishes as the spray distance increases, along with a decrease in the area of high pressure ($p > 80$ MPa). In contrast, high-temperature areas ($T > 150$ °C) occur near the high-pressure zone at the jet center within an annular region, shifting toward the jet center and decreasing in size as spray distance increases. Compared with Fig. 8(a) and (b), the static pressure in the high-temperature region ($T > 150$ °C) is above 1.5 MPa, and the boiling point of water at this pressure is more significant than 150 °C, so the water will not vaporize. The maximum temperature and jet center temperature initially increase and then decrease, reaching the peak value at a spray distance of 10, where the high-temperature area coincides with the jet center. The influence range of impact temperature is more than four times that of impact pressure, indicating that thermal stress will significantly increase the erosion area. From the impact pressure perspective, the larger the spray distance, the lower the jet pressure, indicating that no optimal spray distance exists. Conversely, from the impact temperature perspective, the highest center temperatures are observed near a spray distance of

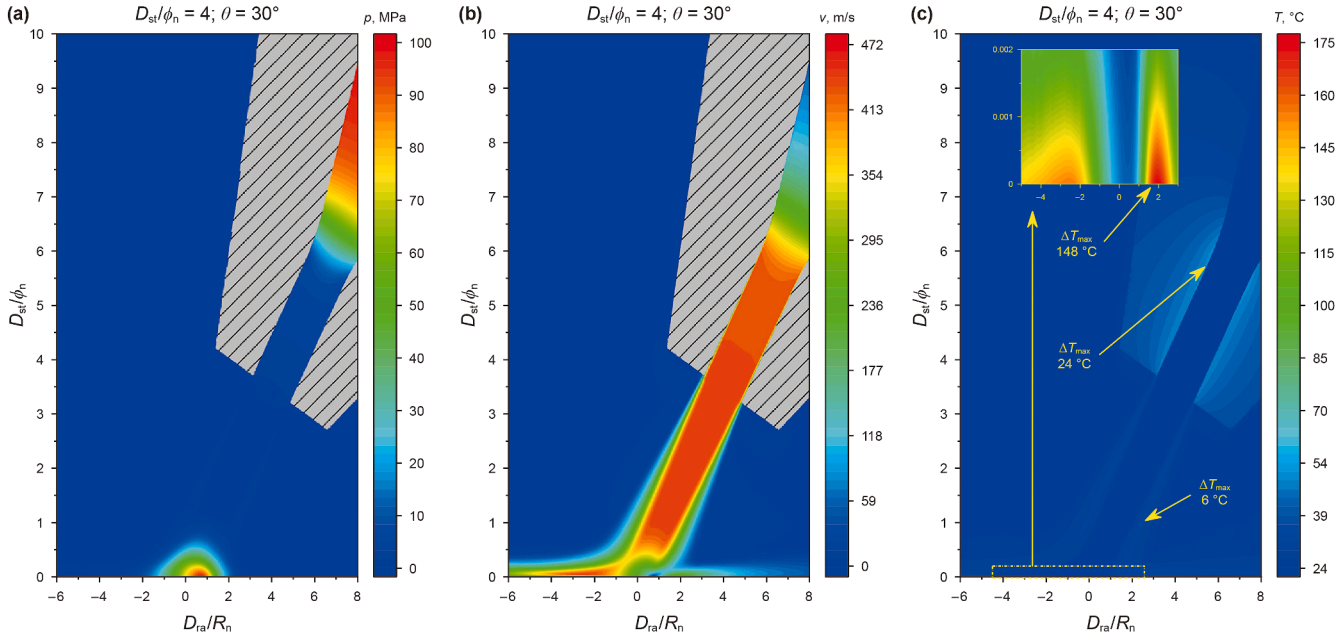

Fig. 5. Impact pressure (**a**), velocity (**b**), and temperature (**c**) contours at a jet angle of 30° for a spray distance of 4.

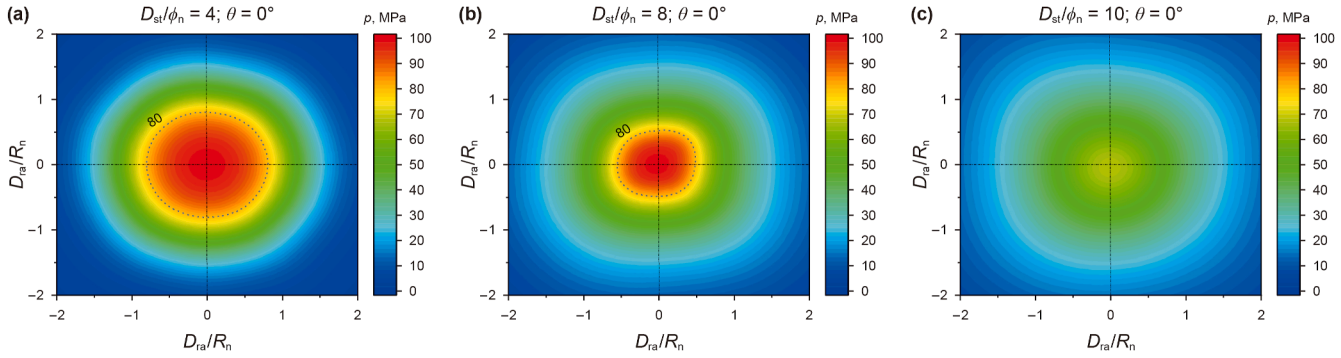

Fig. 6. Impact pressure contours at a jet angle of 0° for spray distances of (**a**) 4, (**b**) 8, and (**c**) 10.

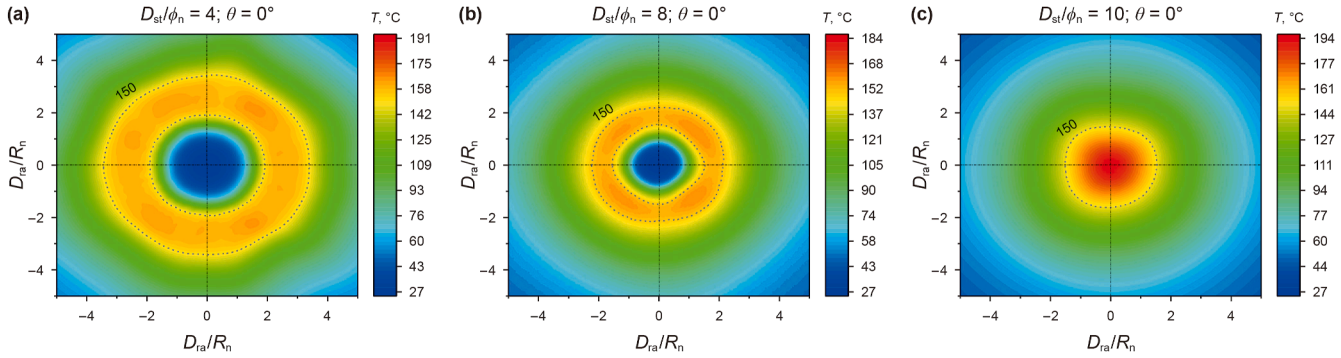

Fig. 7. Impact temperature contours at a jet angle of 0° for spray distances of (**a**) 4, (**b**) 8, and (**c**) 10.

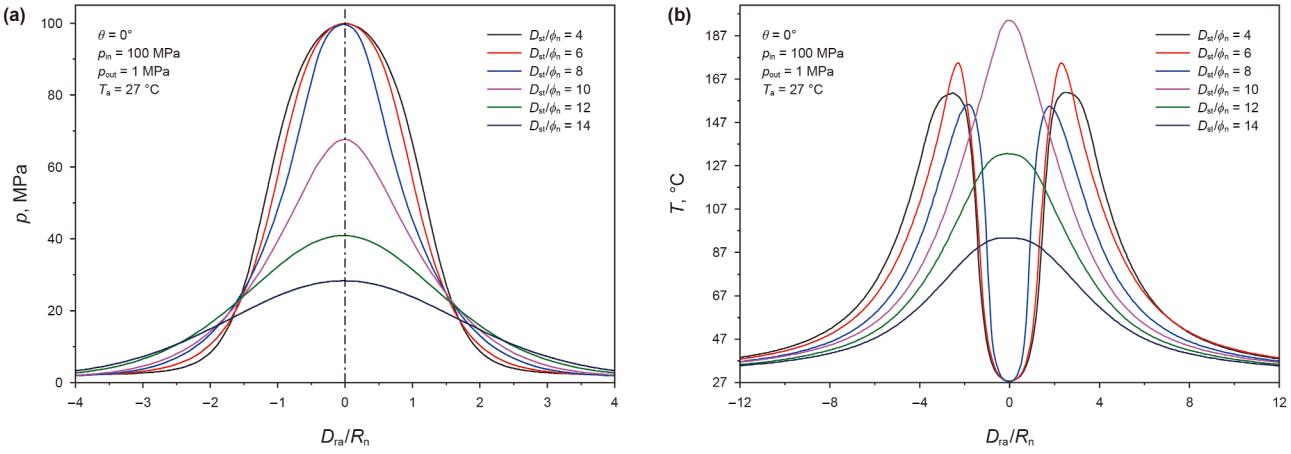

Fig. 8. Impact pressure (**a**) and temperature (**b**) curves from a spray distance of 4–14 at a jet angle of 0°.

10, where jet center impact pressure is also relatively high, indicating a more substantial synergistic effect between impact temperature and pressure on erosion stress; thereby, there is an optimal spray distance. When the spray distance is less than 8, there is no static pressure loss at the jet center ($D_{ra}/R_n = 0$); the dynamic pressure and shear rate are close to zero. The viscous dissipative heating effect is negligible, so the temperature in the jet center is the lowest. When the spray distance exceeds 8, the static pressure of the jet center decreases, and the dynamic pressure and shear rate increase, leading to the rise of the viscous dissipation heating and the jet center temperature. The jet center temperature reaches the maximum value at the spray distance of 10. When the jet distance is greater than 10, the jet energy is lost too much with the spray distance, and the impact pressure becomes smaller, leading to a decrease in the dynamic pressure, shear rate, and viscous dissipation heating effect, and the jet center temperature decreases. When the spray distance is less than 8, the maximum dynamic pressure and shear rate occur near the jet center. When the spray distance exceeds 8, the maximum dynamic pressure and shear rate occur in the jet center. Therefore, as the spray distance increases, the position of the highest temperature moves towards the jet center.

4.3. Variation in impact pressure and temperature with jet angle

Figs. 9 and 10 depict the impact pressure and impact temperature contours at different jet angles for a spray distance of 4, respectively. Figs. 11 and 12 illustrate impact pressure and

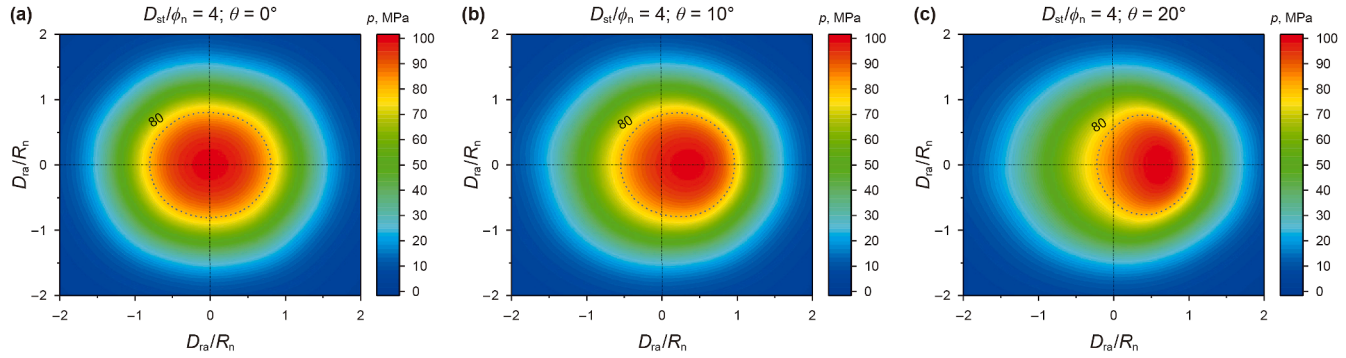

Fig. 9. Impact pressure contours at jet angles of (**a**) 0°, (**b**) 10°, and (**c**) 20° for a spray distance of 4.

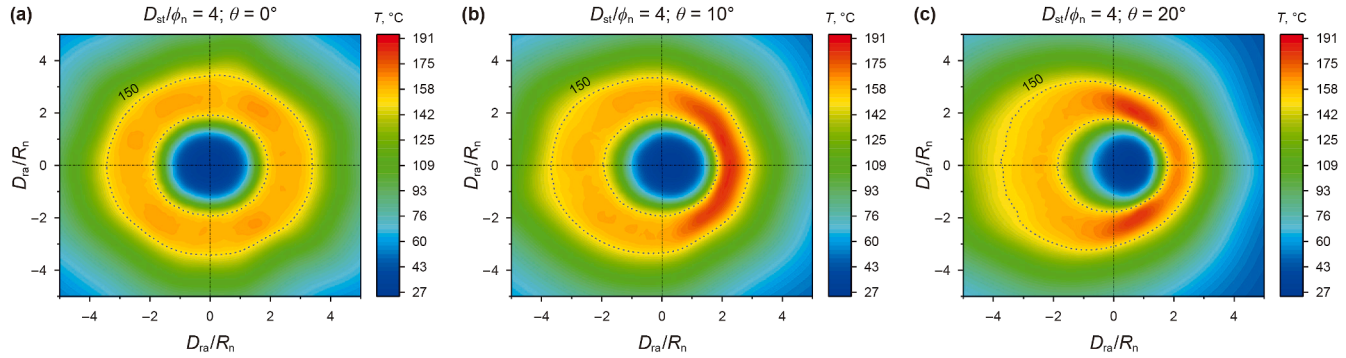

Fig. 10. Impact temperature contours at jet angles of (**a**) 0°, (**b**) 10°, and (**c**) 20° for a spray distance of 4.

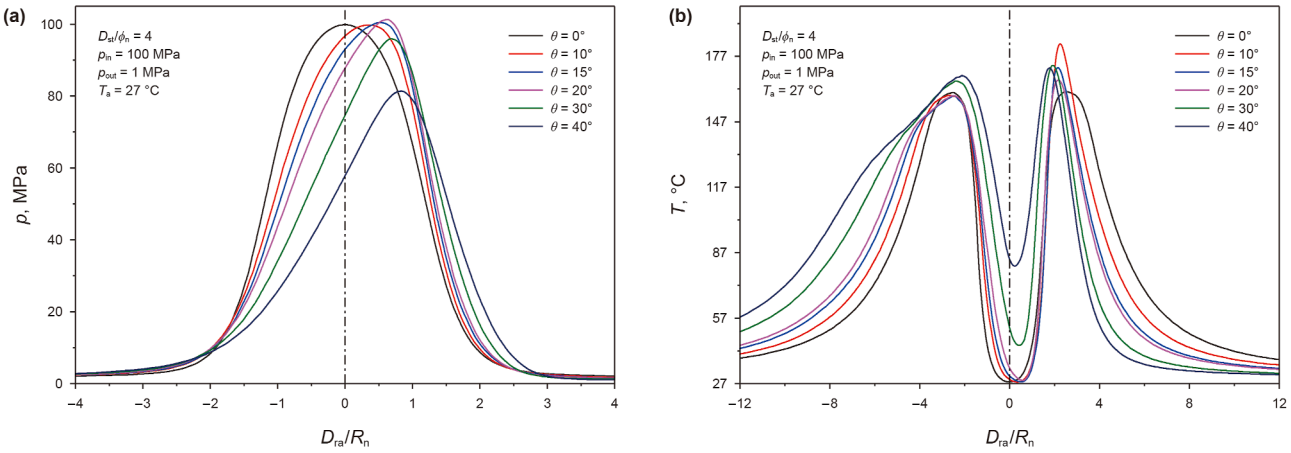

Fig. 11. Impact pressure (**a**) and temperature (**b**) curves at jet angles from 0° to 40° for a spray distance of 4.

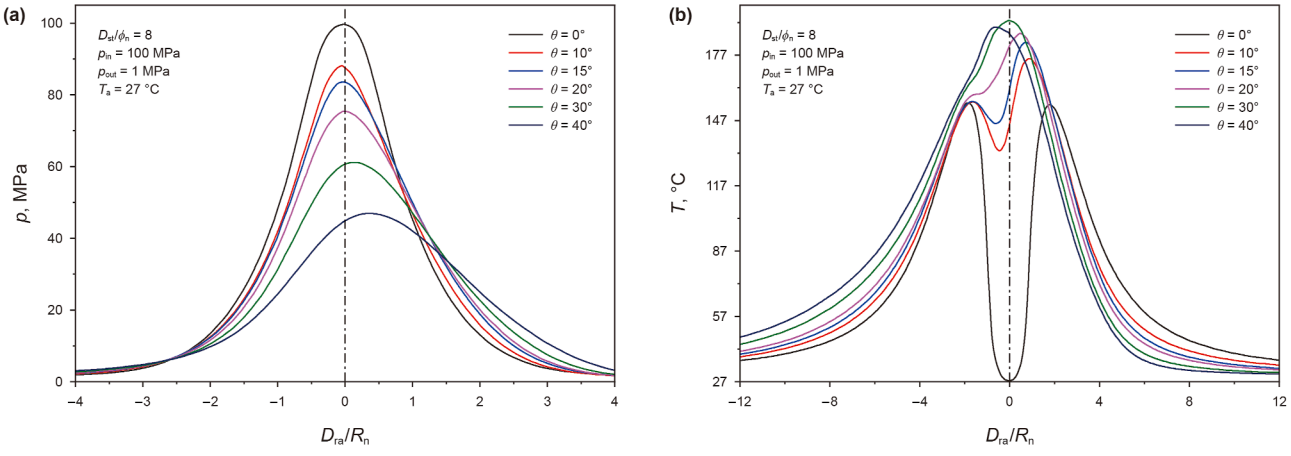

Fig. 12. Impact pressure (**a**) and temperature (**b**) curves at jet angles from 0° to 40° for a spray distance of 8.

temperature curves at spray distances of 4 and 8, respectively, at jet angles from 0° to 40°, in which the horizontal axis represents positions consistent with the incident angle plane. By comparing Figs. 9–12, we can see that as the jet angle increases, the impact pressure decreases, and the high-pressure area shifts to the right side of the jet center; in contrast, the impact temperature increases, and the high-temperature area shifts towards the jet center, reducing the distance between the high-pressure and high-temperature areas. As the spray distance increases from 4 to 8, the impact pressure decreases, while the temperature at different jet angles rises. From the impact pressure analysis, the larger the jet angle, the lower the impact pressure, indicating no optimal jet angles. From the impact temperature analysis, the larger the jet angle, the higher the impact temperature, the closer the distance between the high-pressure and high-temperature areas, suggesting a more substantial synergistic effect between impact temperature and impact pressure on erosion stress, thus indicating the existence of an optimal erosion angle. When the jet angle is 0°,

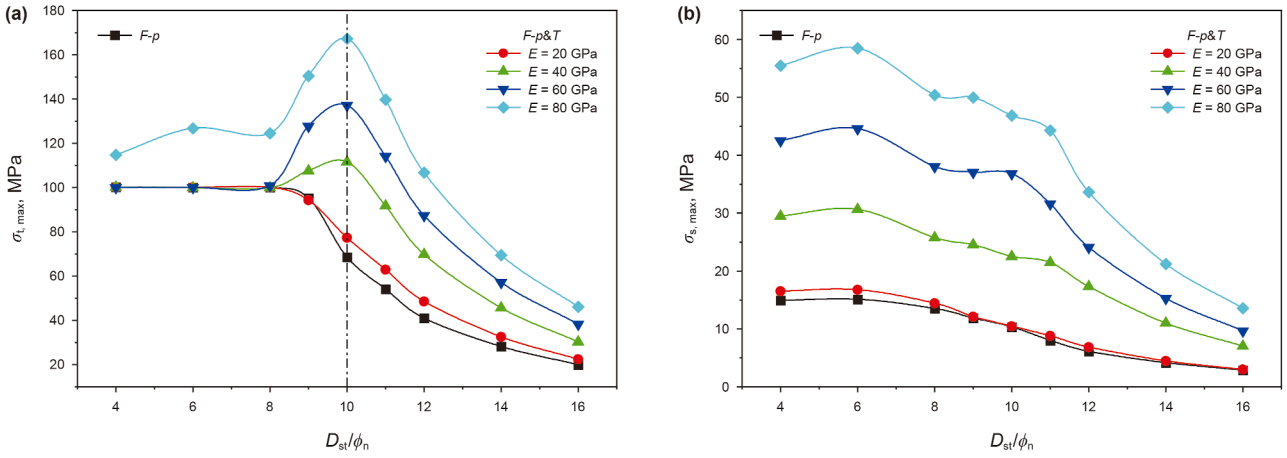

Fig. 13. Variation in the maximum tensile stress (**a**) and shear stress (**b**) with spray distance at a jet angle of 0°.

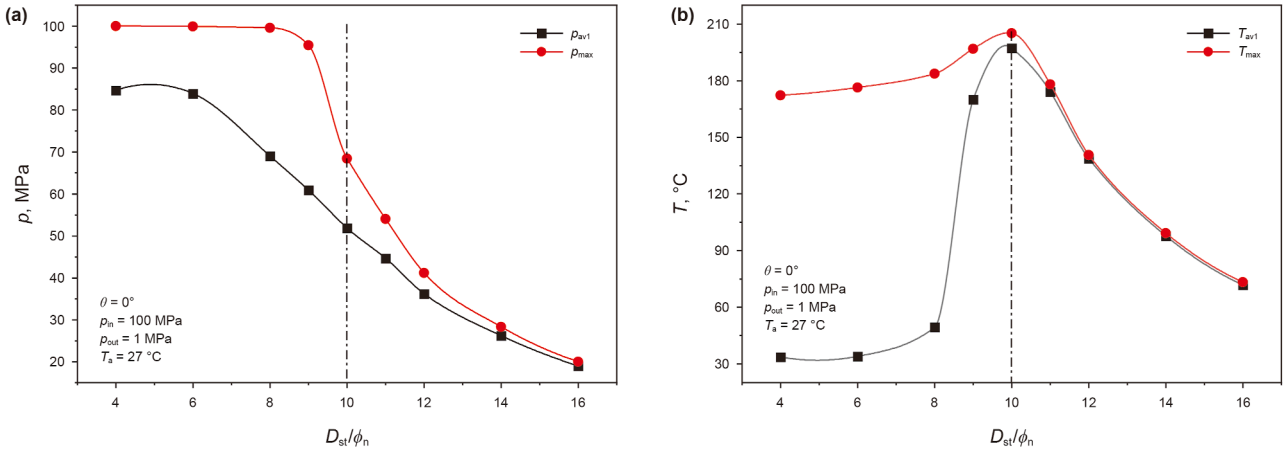

Fig. 14. Variation in the maximum and average impact pressures (**a**) and temperatures (**b**) with spray distance at a jet angle of 0°.

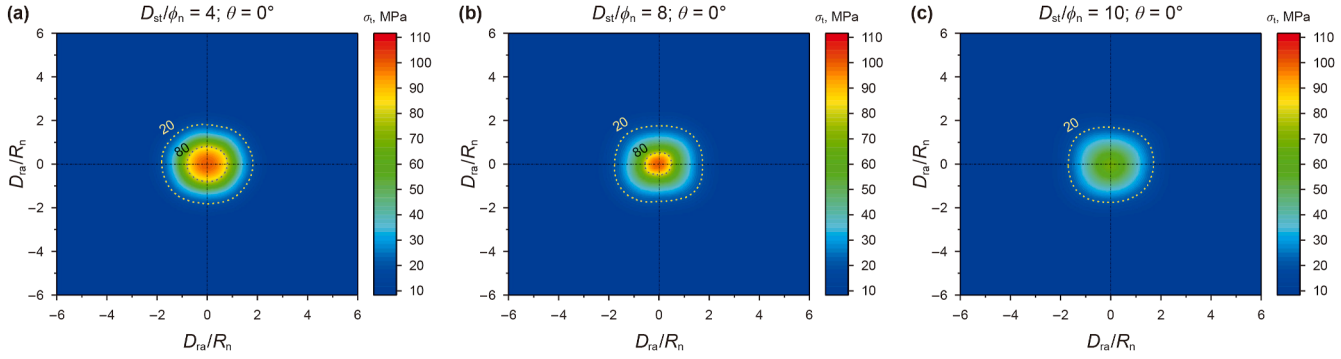

Fig. 15. Tensile stress contours at spray distances of (**a**) 4, (**b**) 8, and (**c**) 10 for a jet angle of 0° and elastic modulus of 40 GPa under pressure field.

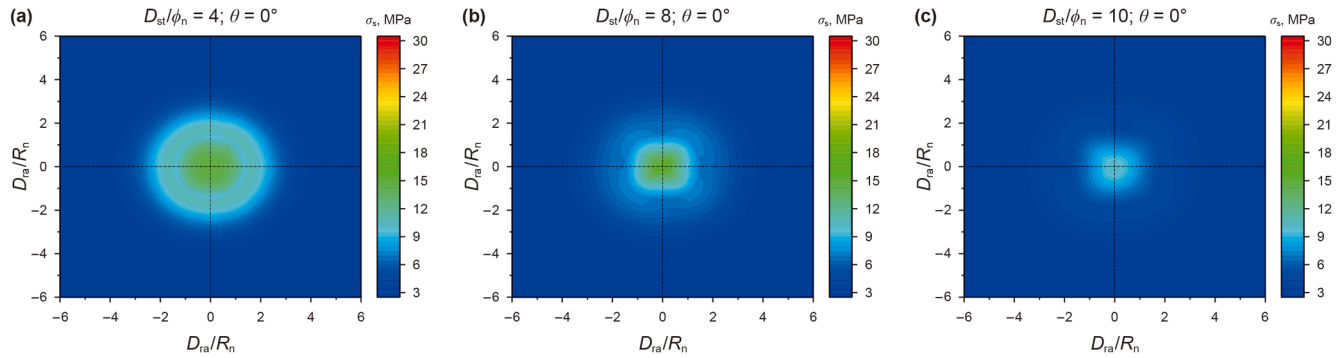

Fig. 16. Shear stress contours at spray distances of (**a**) 4, (**b**) 8, and (**c**) 10 for a jet angle of 0° and elastic modulus of 40 GPa under the pressure field.

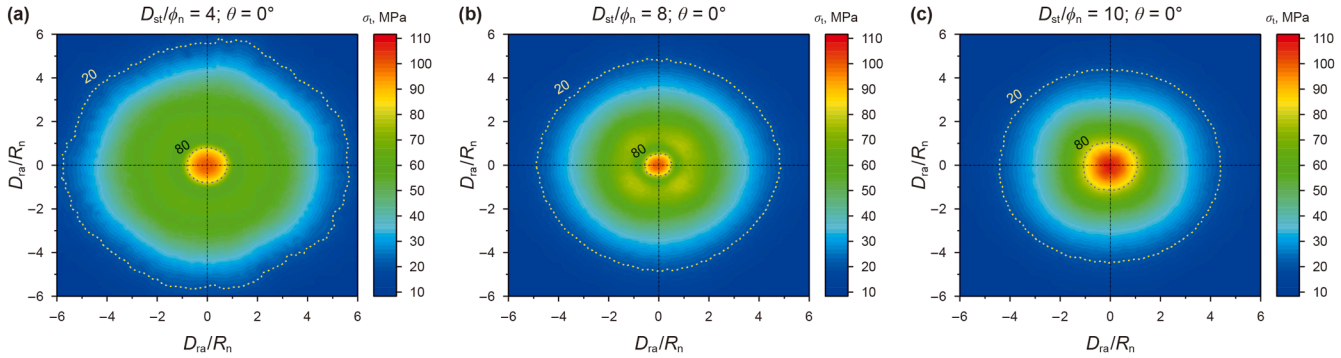

Fig. 17. Tensile stress contours at spray distances of (**a**) 4, (**b**) 8, and (**c**) 10 for a jet angle of 0° and elastic modulus of 40 GPa under temperature-pressure coupling field.

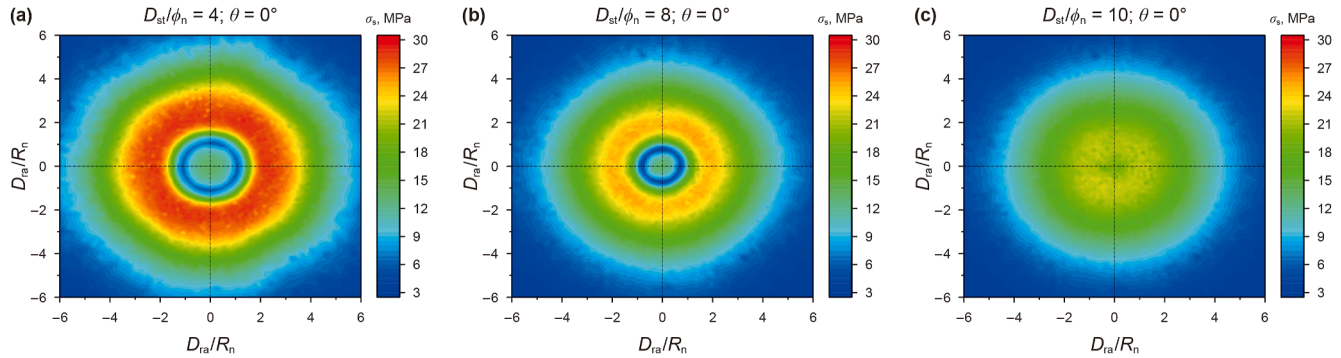

Fig. 18. Shear stress contours at spray distances of (**a**) 4, (**b**) 8, and (**c**) 10 for a jet angle of 0° and elastic modulus of 40 GPa under temperature-pressure coupling field.

there is no loss of static pressure at the jet center ($D_{ra}/R_n = 0$); that is, the dynamic pressure and shear rate are close to zero, and the viscous dissipative heating effect is negligible, so the temperature in the jet center is the lowest. With the increase of jet angle, the static pressure of the jet center decreases, and the dynamic pressure and shear rate increase, which leads to the rise of the viscous dissipation heating effect and the jet center temperature. When the spray distance of 4 becomes 8, the rate of static pressure decay of the jet center is faster with the increase of the jet angle. Therefore, the rise of jet center temperature with the jet angle increases at a spray distance of 8 becomes more considerable.

5. Rock stress variation under the water jet

5.1. Variation in tensile and shear stresses with spray distance

Fig. 13 depicts the variation in maximum tensile stress ($\sigma_{t,\,max}$) and maximum shear stress ($\sigma_{s,\,max}$) on the rock surface at a jet angle of 0° versus the spray distance. It shows that the maximum

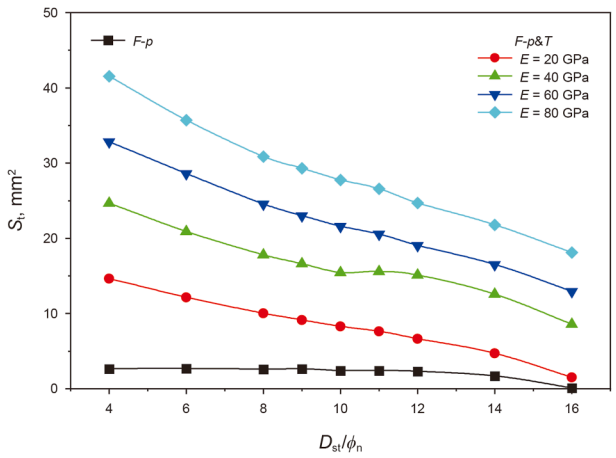

Fig. 19. Variation in the tensile failure area with spray distance and elastic modulus at a jet angle of 0°.

tensile stress exceeds the maximum shear stress by more than threefold. Given the rock's lower tensile strength than its shear strength, tensile damage predominates under jetting conditions. Under the pressure field (*F-p*), the maximum tensile and shear stresses decrease with increasing spray distance, indicating the absence of an optimal spray distance. Conversely, when the elastic modulus is no less than 40 GPa and under the temperature-pressure coupling field (*F-p&T*), the maximum tensile stress first increases, peaking at a spray distance of 10, then diminishes, indicating an optimal spray distance exists. This observation is consistent with the temperature-pressure coupling field analysis presented in Section 4.1. Impact temperatures can nearly double the tensile and shear stresses, emphasizing the pivotal role of thermal stress in water jet erosion. p_{max} and T_{max} denote the

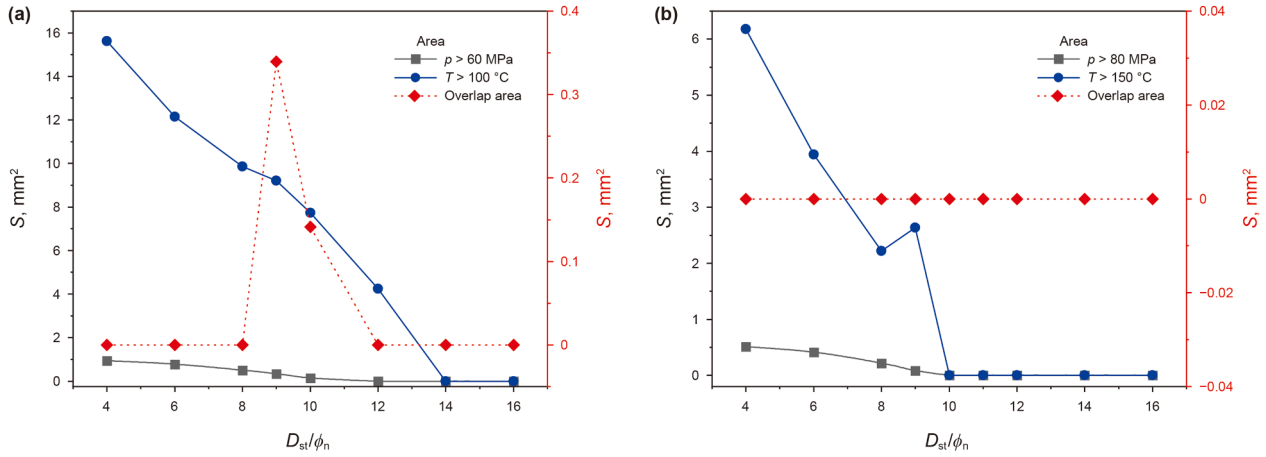

Fig. 20. Variation in high-pressure regions, high-temperature regions, and their overlap regions with spray distance at a jet angle of 0°.

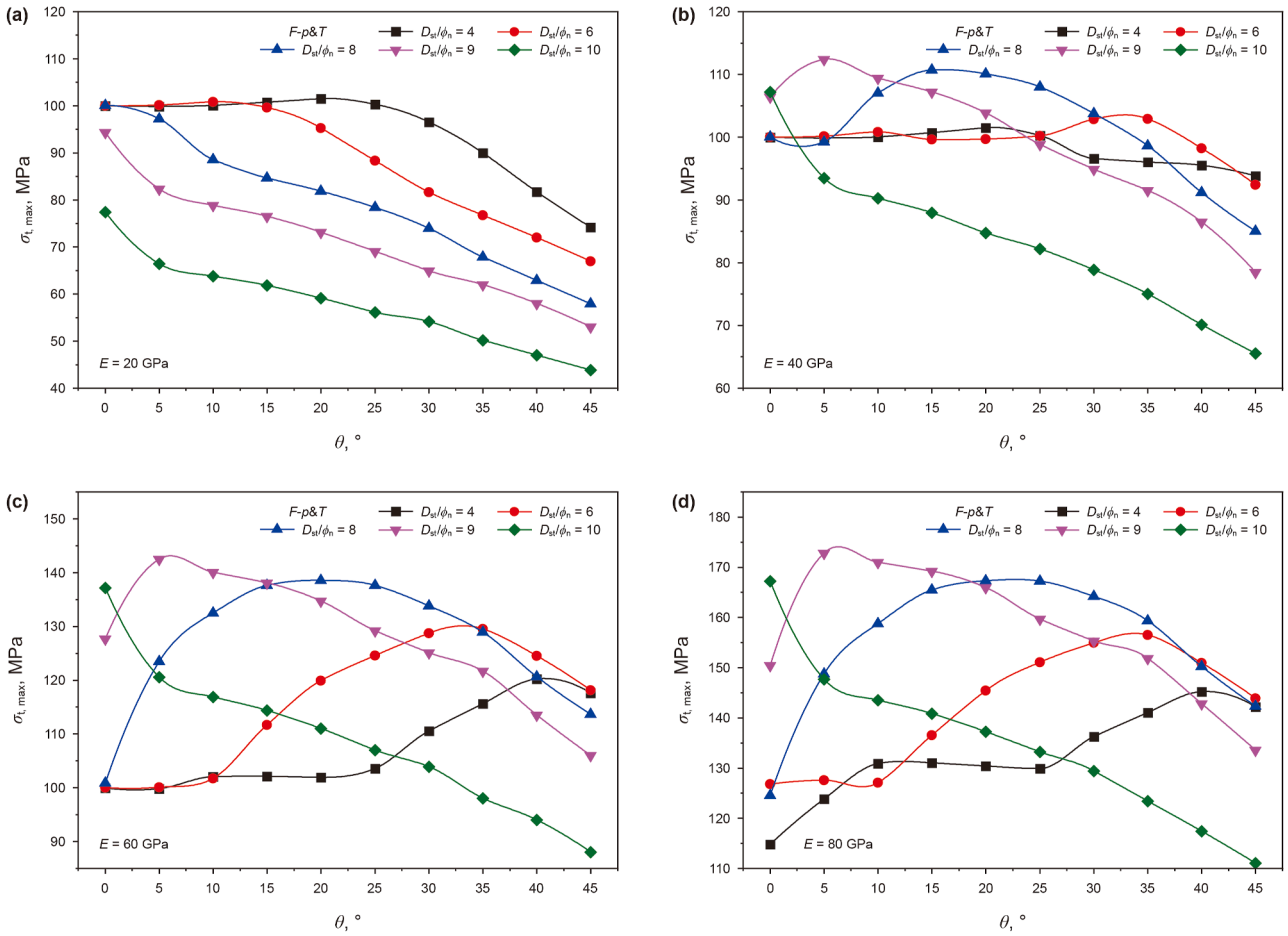

Fig. 21. Variation in maximum tensile stress with jet angle and spray distance when the elastic modulus is (**a**) 20 GPa, (**b**) 40 GPa, (**c**) 60 GPa, and (**d**) 80 GPa under temperature-pressure coupling field.

maximum impact pressure and temperature, respectively, while p_{av1} and T_{av1} represent the average pressure and temperature near the jet center ($D_{ra}/R_n \leq 1$). As shown in Fig. 14, the impact pressure decreases with the increase of the spray distance; however, the impact temperature produces a maximum value at the spray distance of 10, confirming thermal stress as the decisive factor for the optimal erosion spray distance. There is no obvious optimum spray distance for soft rock with the elastic modulus of 20 GPa, showing that the thermal stress effect in the hard rock is larger.

Figs. 15 and 16 show the distribution of tensile and shear stress with the spray distance under the only pressure field, respectively. It can be seen that both the maximum stress and the high stress area are produced at the jet center. Figs. 17 and 18 show the distribution of tensile and shear stress with the spray distance under temperature-pressure coupling field, respectively. It can be seen that the thermal stress has greatly changed the distribution of tensile and shear stress. The high tensile stress ($\sigma_t > 80$ MPa) area still exists at the jet center, but the tensile stress area ($\sigma_t > 20$ MPa) increased 5 times that of the only pressure field. The high shear stress area is annular, occurring near the jet center, and moves toward the jet center as the spray distance increases. When the spray distance is 10, high tensile stress and high shear stress zones are produced in the jet center, resulting in a strong tension-shear coupling failure effect. By comparing Figs. 6 and 7, it is evident that at a spray distance of 10, the tensile stress is more significantly influenced by the temperature field. When the spray distance is 4–8, the shear stress is more affected by the temperature field.

Using the tensile stress of 20 MPa as a criterion for the tensile failure area (S_t), Fig. 19 is the variation in the tensile failure area with spray distance and elastic modulus at a jet angle of 0°, showing that the tensile failure area (S_t) decreases with the spray distance. When the spray distance is 10, both the maximum tensile stress ($\sigma_{t,\ max}$) and the high tensile stress region ($\sigma_t > 80$ MPa) appear. Therefore, considering that the tensile failure area (S_t), the optimal spray distance of hard rock ($E \geq 40$ GPa) should be less than 10. Fig. 20 is the overlap region of the high pressure and high temperature with spray distance at a jet angle of 0°. It can be seen that both the high-pressure zone and the high-temperature zone decrease with the increase of the spray distance, which cannot explain the reason for the occurrence of the maximum tensile stress at the spray distance of 10. However, the overlapping area of the high-pressure zone and the high-temperature zone shows a peak at the spray distance of 10, corresponding to the maximum tensile stress at the spray distance of 10, indicating that the larger the overlapping area, the stronger the coupling effect of the temperature field and the pressure field against the erosion stress. From the perspective of stress and strain, the high-pressure area at the jet center forces the rock particles to migrate to both sides of the center, forming a radial displacement field, that is, the radial extrusion effect. The high-temperature zone of the jet will cause thermal expansion strain in the rocks near the center of the jet, which will increase the radial extrusion effect of the jet pressure. Therefore, as the overlap degree between the areas of high-pressure and high-temperature increases, the coupling strain of

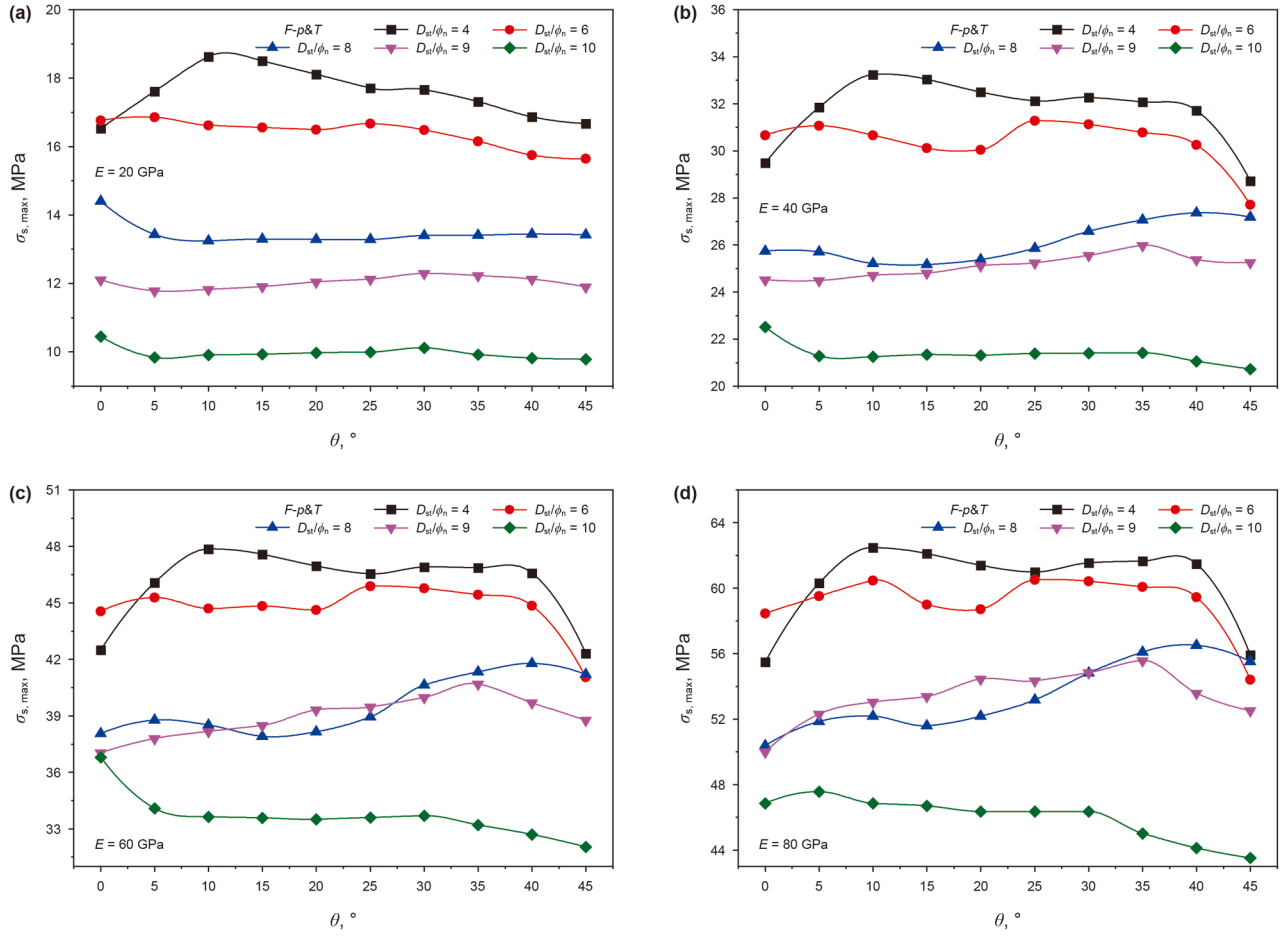

Fig. 22. Variation in maximum shear stress with jet angle and spray distance when the elastic modulus is (**a**) 20 GPa, (**b**) 40 GPa, (**c**) 60 GPa, and (**d**) 80 GPa under temperature-pressure coupling field.

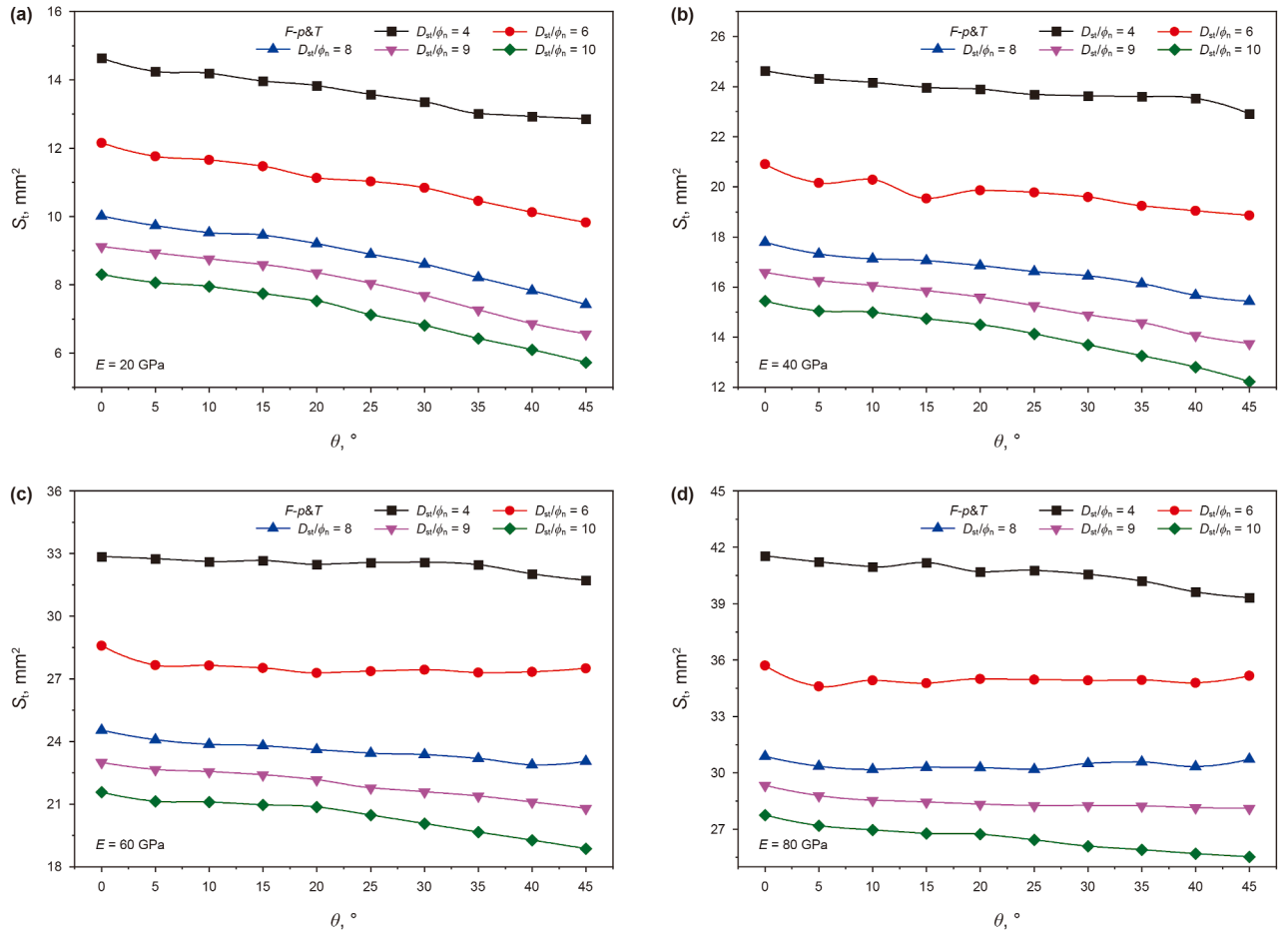

Fig. 23. Variation in tensile failure area with jet angle and spray distance when the elastic modulus is (**a**) 20 GPa, (**b**) 40 GPa, (**c**) 60 GPa, and (**d**) 80 GPa.

the jet pressure and temperature increases, and the erosion stress increases.

5.2. Variation in tensile and shear stresses with jet angle

Figs. 21 and 22 show the variation in maximum tensile stress and maximum shear stress with jet angle, spray distance, and elastic modulus under the temperature-pressure coupling field and pressure field, respectively. The maximum tensile stress is nearly 8 times the maximum shear stress, and the maximum shear stress does not obviously change with the jet angle; therefore, the maximum tensile stress is the key factor to determine the optimal jet angle. When the elastic modulus is 20 GPa, the maximum tensile stress has no obvious peak value with the increase of jet

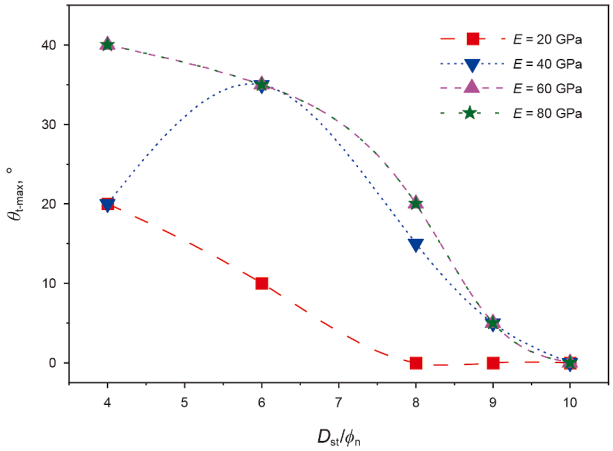

Fig. 24. Variation in the optimum jet angle with spray distance when the elastic modulus is 20, 40, 60, and 80 GPa.

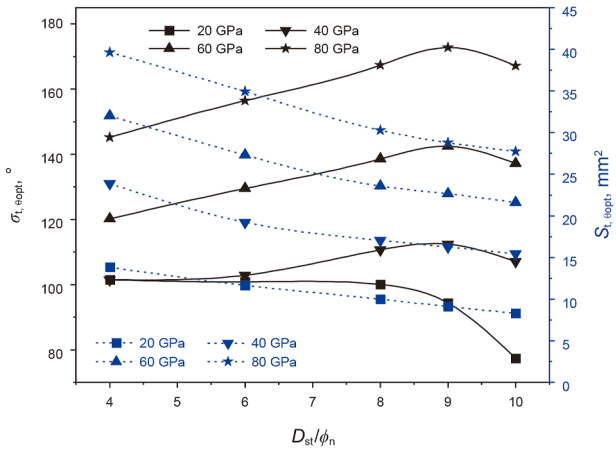

Fig. 25. Variation in the maximum tensile stress ($\sigma_{t,\ \theta opt}$) and tensile failure area ($S_{t,\ \theta opt}$) with spray distance when the elastic modulus is 20, 40, 60, and 80 GPa.

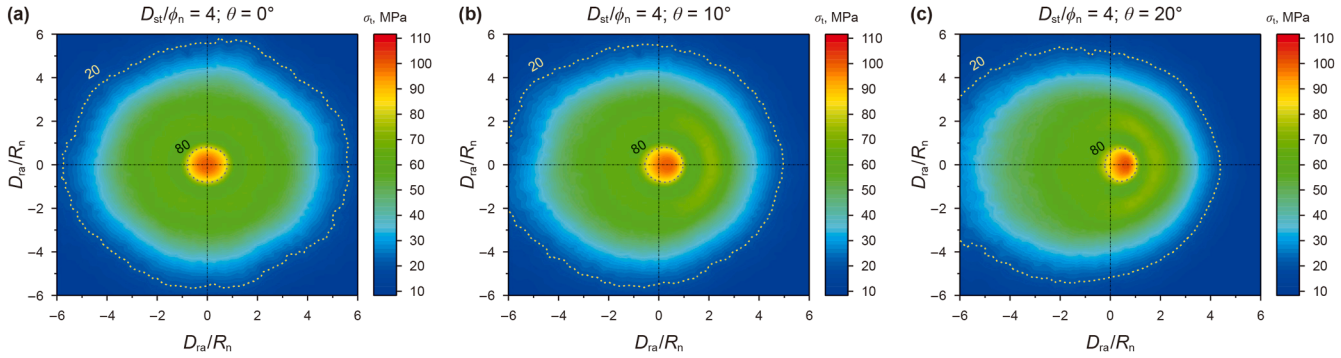

Fig. 26. Tensile stress contours at a spray distance of 4 and elastic modulus of 40 GPa when the jet angle is (**a**) 0°, (**b**) 10°, and (**c**) 20°.

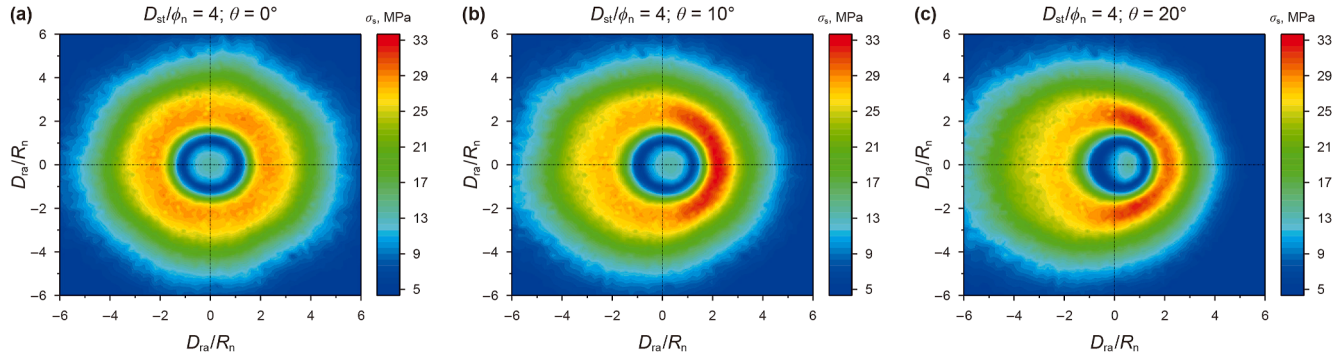

Fig. 27. Shear stress contours at a spray distance of 4 and elastic modulus of 40 GPa when the jet angle is (**a**) 0°, (**b**) 10°, and (**c**) 20°.

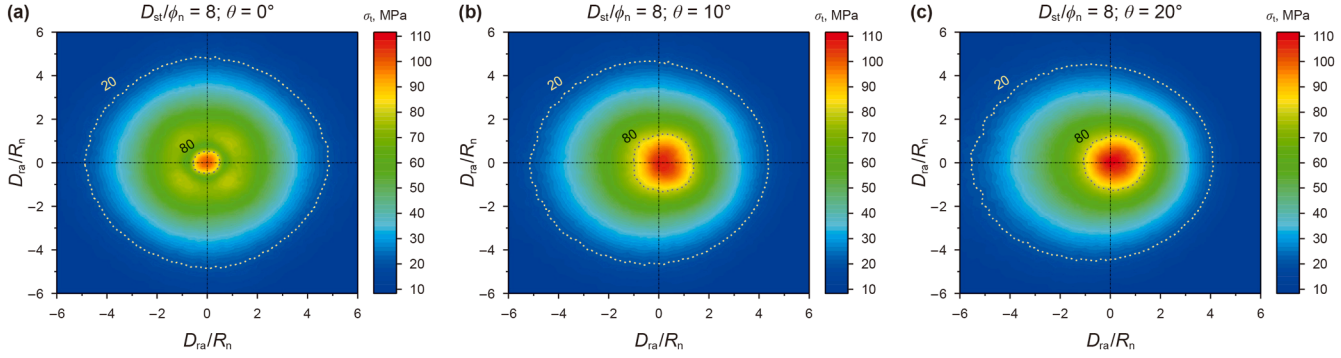

Fig. 28. Tensile stress contours at a spray distance of 8 and elastic modulus of 40 GPa when the jet angle is (**a**) 0°, (**b**) 10°, and (**c**) 20°.

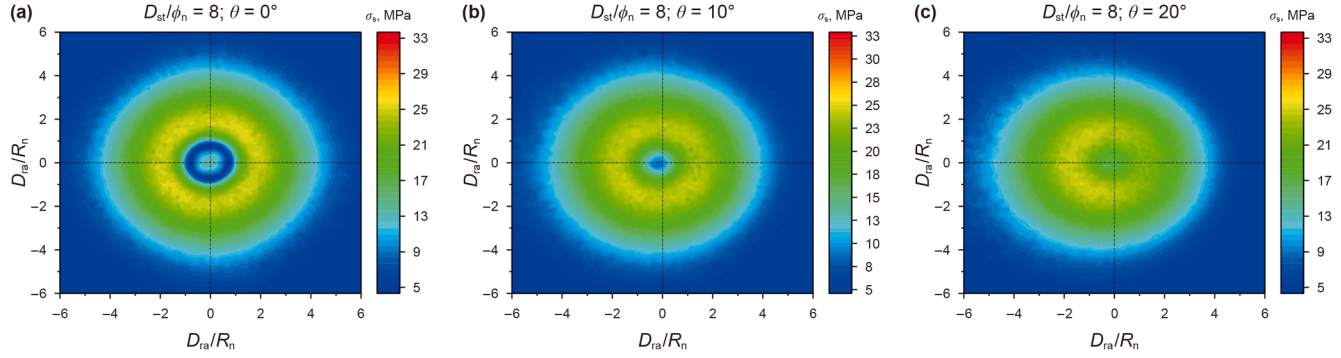

Fig. 29. Shear stress contours at a spray distance of 8 and elastic modulus of 40 GPa when the jet angle is (**a**) 0°, (**b**) 10°, and (**c**) 20°.

angle. When the elastic modulus is greater than or equal to 40 GPa, the maximum tensile stress first increases and then decreases, indicating the existence of an optimal jet angle in hard rock. Fig. 23 shows the variation in the tensile failure area (S_t) with jet angle and spray distance, indicating that the tensile failure area decreases with the increase of jet angle and spray distance. Taking the maximum tensile stress ($\sigma_{t,\ max}$) as the criterion, Fig. 24 shows the variation in the optimal jet angle with the spray distance and elastic modulus. It can be seen that the optimal jet angle decreases with the increase of spray distance and increases with the increase of elastic modulus in the range of 0° to 45°. Fig. 25 shows the contours in maximum tensile stress ($\sigma_{t,\ \theta opt}$) and tensile failure area ($S_{t,\ \theta opt}$) with the spray distance at the optimal jet angle. The results show that for soft rock ($E = 20$ GPa), the best choice to reduce the threshold pressure of water jet rock-breaking is a spray distance of 4 and a jet angle of 20°. For hard rock ($E \geq 40$ GPa) and fast-moving nozzle conditions, the spray distance of 9° and jet angle of 15°–20° can reduce the jet rock-breaking threshold pressure mostly. If the jet time is increased, a smaller spray distance and jet angle should be selected to increase the tensile failure depth. Figs. 26 and 28 show the distribution of tensile stress under different jet angles when the spray distance is 4 and 8, respectively. When the jet angle increases, the high tensile stress zone ($\sigma_t > 80$ MPa) moves toward the nozzle inclination direction, while the tensile failure zone ($\sigma_t > 20$ MPa) moves in the opposite direction, which is consistent with the pressure and temperature distribution in Figs. 9 and 10. In general, the high tensile stress zone at a spray distance of 8 is larger than that at a spray distance of 4, while the tensile failure zone shows the opposite trend. Therefore, it is necessary to optimize the spray distance and jet angle to reduce the threshold pressure of the jet rock-breaking or increase the area of the jet rock-breaking. Figs. 27 and 29 show shear stress distribution under different jet angles when the spray distance is 4 and 8, respectively. The results show that the high shear stress zone at a spray distance of 4 is larger than that at a spray distance of 8, while the overlap zone of high shear stress and high tensile stress presents the opposite trend, indicating that increasing the spray distance can enhance the coupling erosion effect of temperature and pressure at different jet angles. Compared with Figs. 10 and 27, the distribution of high shear stress is similar to that of high temperature, indicating that the region of high shear stress is mainly affected by the temperature field. Fig. 30 shows the contours in average impact pressure and average impact temperature with jet angle at different spray distances. The impact pressure decreases with the increase of jet angle, but the impact temperature varies greatly. When the spray distance is 4 and 6, the impact temperature continues to rise. When the spray distance is 8 or 9, the impact temperature increases first and then decreases. When the spray distance is 10, the impact temperature continues to decrease. Combining Figs. 11 and 12, it can be seen that when the maximum pressure loss is approximately 40 MPa, the temperature at the jet center is the highest. Therefore, the loss of jet pressure at a bigger spray distance is faster, and the jet angle producing the maximum temperature is smaller. The temperature contour is consistent with the trend of maximum tensile stress decreasing with the increase of jet angle shown in Fig. 21, indicating that thermal stress is the key factor determining the optimal jet angle. Fig. 31 is the overlap region of the high pressure and high temperature with jet angle at spray distances of 4 and 8. We can see that the high-pressure zone decreases with the increase of the jet angle, but the contour of the high-temperature zone with jet angle is chaotic, which cannot explain the existence of an optimum jet angle. However, the overlapping area of the high-pressure zone and the high-temperature zone shows a peak at a jet angle of 40° and 10° for the spray distances of 4 and 8, respectively. The variation in the overlap region between the high-pressure and the high-temperature corresponds to the non-zero optimal jet angle (Fig. 24), indicating that the overlap region is a key factor affecting the optimal jet angle. However, the correspondence is not precise. This is because the temperature varies irregularly with the jet angle, and the coupling between the temperature and pressure fields is more complex. For instance, when the spray distance is 8 and the jet angle is 20°, the area of the high-temperature zone above 150 °C is the largest, and the maximum tensile stress ($E \geq 40$ GPa) at this time is also the greatest, while the overlapping area between 150 °C and 80 MPa is not the largest. From the perspective of strain and stress, the influence of temperature and pressure on erosion stress is affected by three aspects. The first is the maximum pressure and the maximum temperature. The second is the overlap region of the high-pressure and the high-temperature. The third is the area of the high-pressure region and the high-temperature region. The greater the impact pressure and temperature, the higher the upper limit of the maximum stress under the coupling of temperature and pressure fields. The higher the overlap degree between the high-temperature zone and the high-pressure zone, the greater the coupling effect of the temperature and pressure fields on stress. The larger the area of the high-temperature region and the high-pressure region is, the greater the cumulative strain over a wider range can be generated on the impact surface, and the erosion stress will also increase. However, from the perspective of increasing the area of rock-

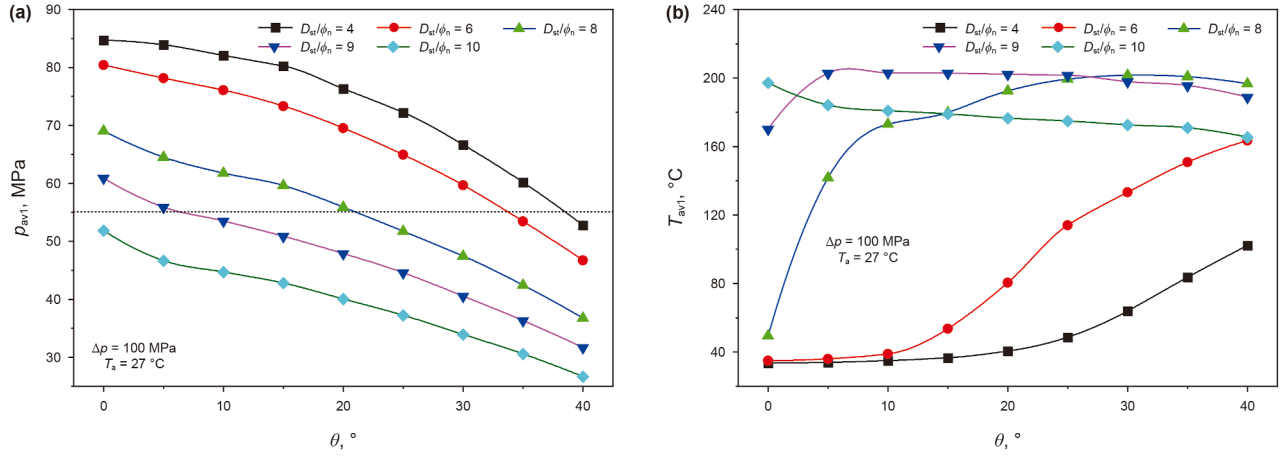

Fig. 30. Variation in average impact pressures (**a**) and average impact temperatures (**b**) with the jet angle at spray distances of 4, 6, 8, 9, and 10.

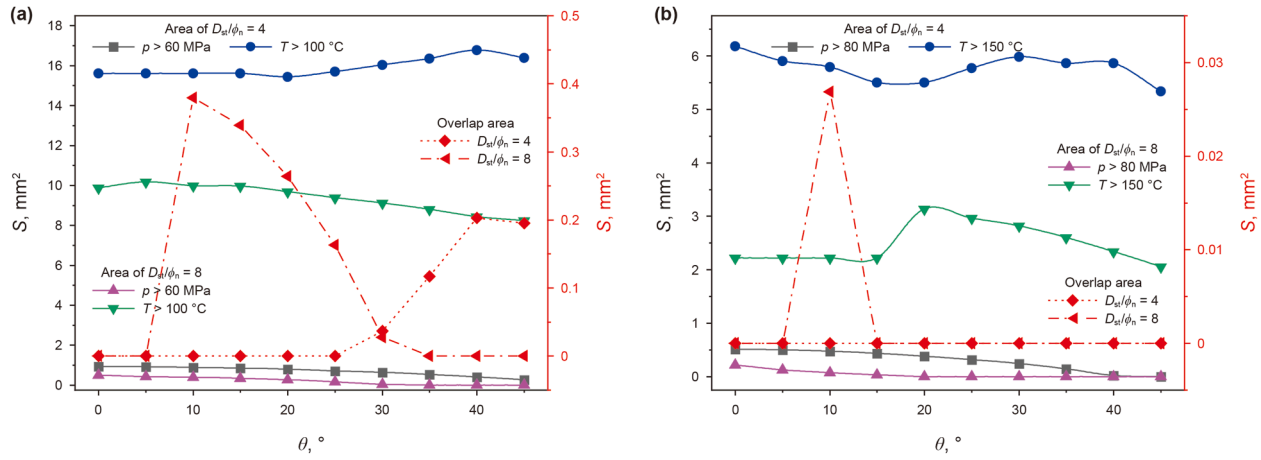

Fig. 31. Variation in high-pressure regions, high-temperature regions, and their overlap regions with jet angle at spray distances of 4 and 8.

breaking, the smaller the jet distance and the jet angle, the better. At this time, the rock-breaking stress at the center of the jet ($D_{ra}/R_n < 2$) is generated by the pressure field, and the rock-breaking stress near the center of the jet ($D_{ra}/R_n > 2$) is generated by the temperature field, which can significantly increase the rock-breaking area. Overall, the maximum rock-breaking stress and the rock-breaking area cannot be achieved simultaneously. It is necessary to adjust the spray distance and jet angle in combination with the on-site requirements.

6. Conclusion

(1) The impact temperature of the water jet generated under viscous dissipation is a key factor affecting the erosion area, optimal spray distance, and jet angle. The impact temperature of a 100 MPa water jet can be more than 150 °C, the area of the high-temperature zone is more than 4 times that of the high-pressure zone, and the thermal stress increases the erosion stress by more than 1 times. Under the temperature-pressure coupling field, although the increase of thermal stress is larger than that of shear stress, the rock is still dominated by tensile failure.

(2) With the increase of the spray distance, the impact pressure decreases, the impact temperature rises first and then falls, the high-temperature area transfers to the high-pressure area in the jet center, and the overlapping area of the two increases. Therefore, there is no optimal spray distance under a pressure-only field or when the rock elastic modulus is low. Under the temperature-pressure coupling field and when the rock elastic modulus is high, the maximum tensile stress increases first and then decreases, and reaches the peak value when the spray distance is 10. There is an optimal spray distance.

(3) When the spray distance is less than 10, the impact pressure decreases with the increase of jet angle, but the impact temperature increases, and the overlap region between the high temperature and the high pressure increases. Therefore, when only the pressure field acts, the optimal jet angle (non-zero) doesn't exist, while under the temperature-pressure coupling field, the maximum tensile stress first increases and then decreases, and the optimal jet angle exists. The optimal jet angle varies from 0° to 40° influenced by the spray distance and elastic modulus. It decreases with the increase of the spray distance and increases with the increase of the elastic modulus. For hard rock ($E \geq 40$ GPa) and fast-moving nozzle conditions, the jet erosion threshold pressure can be effectively reduced by the spray distance of 9 and the jet angle of 15°–20°.

(4) The spray distance and the jet angle can adjust the overlap region between zones of high-pressure and high-temperature. As the overlap region increases, the coupling effect of temperature and pressure increases, which can reduce the threshold pressure of the jet-breaking rock. When the overlap region decreases, the area affected by the temperature and pressure fields increases, which can increase the rock-breaking area.

(5) Current research on high-pressure jet rock-breaking mainly focused on pure water jets. However, in petroleum drilling, the viscosity of drilling fluid is generally more than 30 times that of pure water. The potential core of the jet passing through the drill bit nozzle is shorter, and the impact temperature and heat-fluid-solid coupling stress increase with the viscosity increase. The optimal jet angle will also vary significantly with the spray distance change. Therefore, future research on jet rock-breaking stress should be based on the rheological properties of drilling fluid to reduce the jet pressure.

CRediT authorship contribution statement

Mu-Kun Li: Writing – original draft, Methodology, Funding acquisition, Data curation, Conceptualization. **Cai-Yun Xiao:** Writing – review & editing, Validation, Software, Resources, Conceptualization. **Xue Sun:** Writing – review & editing, Validation, Methodology, Funding acquisition. **Hong-Jian Ni:** Validation, Supervision, Conceptualization. **Yu-Kun Du:** Validation, Software, Resources.

Data availability

All data in this study are available upon request by contacting the corresponding author.

Declaration of competing interest

The authors declare that they have no known competing financial interests or personal relationships that could have appeared to influence the work reported in this paper.

Acknowledgement

This work was supported by the National Natural Science Foundation of China (No. 52204126) and the Shandong Provincial Natural Science Foundation (Nos. ZR2022ME077, ZR2022QE060, and ZR2023ME119).

Nomenclature

C	Rock capacity, J/(kg·K)
D_{ra}	The radial distance between a point on the rock surface and the center of the jet, mm
D_{ra}/R_n	The dimensionless radius distance, dimensionless
D_{st}	The spray distance between the nozzle and rock surface, mm
D_{st}/ϕ_n	The dimensionless spray distance, dimensionless
E	Modulus of elasticity, Pa
EW	Aluminum erosion weight, mg
K_s	The surface roughness, 10^{-6} m
p	Fluid pressure, MPa
p_{av1}	The average pressure near the center of the jet ($D_{ra}/R_n \leq 1$), MPa
$p_{dr,\ exp}$	Loss ratio of experimental jet center pressure, dimensionless
$p_{dr,\ tube}$	Loss ratio of simulated jet center pressure, dimensionless
p_{max}	Maximum impact pressure of rock surface, MPa
q_v	Heat generation rate, J/(m^3·s)
R_n	Nozzle diameter, mm
S	Area of given conditions, mm^2
S_t	Tensile failure area under tensile strength of 20 MPa, mm^2
$S_{t,\ \theta opt}$	Tensile failure area at the optimal jet angle, mm^2
t	Time, s
t_j	Jet time, s
T	Rock or fluid temperature, °C
T_{av1}	The average temperature near the center of the jet ($D_{ra}/R_n \leq 1$), °C
T_{max}	Maximum impact temperature of rock surface, °C
T_0	Initial rock temperature, °C
ΔT_{max}	Maximum temperature contour, °C
v	Flow velocity of the fluid, m/s
υ	Poisson's ratio, dimensionless
ϕ_n	The radius of the nozzle, mm
θ	Jet angle degree, °
ρ	Rock or fluid density, kg/m^3
λ	Heat conductivity, W/(m·K)
α	Thermal expansion coefficient, K^{-1}
ε_{ii}	Strain in direction i, dimensionless
σ_{ii}, σ_{jj}, σ_{ll}	Stress tensor in three directions on the coordinate, Pa
$\sigma_{s,\ max}$	Maximum shear stress, MPa
$\sigma_{t,\ max}$	Maximum tensile stress, MPa
$\sigma_{t,\ \theta opt}$	Maximum tensile stress at the optimal jet angle, MPa

References

Beentjes, I., Bender, J.T., Hillson, S.D., et al., 2018. Hydrothermal spallation of barre granite using supercritical water jets. In: Proceedings, 43rd Workshop on Geothermal Reservoir Engineering. Stanford University, Stanford, California.

Cai, C., Li, B.R., Zhang, Y.Y., et al., 2022. Fracture propagation and induced strain response during supercritical CO_2 jet fracturing. Pet. Sci. 19 (4), 1682–1699. https://doi.org/10.1016/j.petsci.2022.03.019.

Chen, J.X., Yang, R.Y., Huang, Z.W., et al., 2022. Detached eddy simulation on the structure of swirling jet flow field. Petrol. Explor. Dev. 49 (4), 806–817. https://doi.org/10.1016/S1876-3804(22)60322-7.

Chen, Q.P., Ji, H., Zhao, H.K., et al., 2020. Optimization algorithm and joint simulation to micro thermal deformation using temperature measurement in the orifice of hydraulic valve. Processes 8 (9), 1136. https://doi.org/10.3390/pr8091136.

Chen, Q.P., Ji, H., Xing, H.H., et al., 2021. Experimental study on thermal deformation and clamping force characteristics of hydraulic spool valve. Eng. Fail. Anal. 129, 105698. https://doi.org/10.1016/j.engfailanal.2021.105698.

Čuha, D., Hatala, M., 2022. Effect of a modified impact angle of an ultrasonically generated pulsating water jet on aluminum alloy erosion using upward and downward stair trajectory. Wear 500, 204369. https://doi.org/10.1016/j.wear.2022.204369.

Dahiya, A.K., Bhuyan, B.K., Kumar, S., 2022. Perspective study of abrasive water jet machining of composites — a review. J. Mech. Sci. Technol. 36 (1), 213–224. https://doi.org/10.1007/s12206-021-1220-x.

Deng, J., Shao, X.M., Fu, X., et al., 2009. Evaluation of the viscous heating induced jam fault of valve spool by fluid–structure coupled simulations. Energy Convers. Manag. 50 (4), 947–954. https://doi.org/10.1016/j.enconman.2008.12.033.

Hu, P., Li, Y., Han, Y., et al., 2016. Numerical simulations of the mean wind speeds and turbulence intensities over simplified gorges using the SST k-ω turbulence model. Engin App Computational Fluid Mech 10 (1), 359–372. https://doi.org/10.1080/19942060.2016.1169947.

Hu, X., Song, X., Liu, Y., et al., 2019. Lowest required surface temperature for thermal spallation in granite and sandstone specimens: experiments and simulations. Rock Mech. Rock Eng. 52 (6), 1689–1703. https://doi.org/10.1007/s00603-018-1665-0.

Huang, F., Zhao, Z., Li, D., et al., 2022. Investigation of the breaking manifestations of bedded shale impacted by a high-pressure abrasive water jet. Powder Technol. 397, 117021. https://doi.org/10.1016/j.powtec.2021.11.065.

Huang, Z.W., Wu, X.G., Li, R., et al., 2019. Mechanism of drilling rate improvement using high-pressure liquid nitrogen jet. Petrol. Explor. Dev. 46 (4), 810818. https://doi.org/10.1016/S1876-3804(19)60239-9.

Kestin, J., Sengers, J., Kamgar-Parsi, B., et al., 1984. Thermophysical properties of fluid H_2O. J. Phys. Chem. Ref. Data 13 (1), 175–183. https://doi.org/10.1063/1.555707.

Kobayashi, R., Arai, T., Yamada, H., 1987. Structure of a water jet and the damage process of metals in jet cutting technology. Trans. Japan Soc. Mech. Engineers 53, 1539–1542.

Li, G.S., Sheng, M., Tian, S.C., et al., 2012. Multistage hydraulic jet acid fracturing technique for horizontal wells. Petrol. Explor. Dev. 39 (1), 100–104. https://doi.org/10.1016/S1876-3804(12)60021-4.

Li, G.S., Huang, Z.W., Tian, S.C., et al., 2010. Research and application of water jet technology in well completion and stimulation in China. Pet. Sci. 7 (2), 239–244. https://doi.org/10.1007/s12182-010-0009-9.

Li, M.K., Ni, H., Cao, Y.G., et al., 2020. Flow energy transformation and dissipation mechanisms of carbon dioxide, nitrogen, and water jets. J. Nat. Gas Sci. Eng. 84, 103650. https://doi.org/10.1016/j.jngse.2020.103650.

Li, M.K., Ni, H.J., Wang, G., et al., 2017a. Simulation of thermal stress effects in submerged continuous water jets on the optimal standoff distance during rock breaking. Powder Technol. 320, 445–456. https://doi.org/10.1016/j.powtec.2017.07.071.

Li, M.K., Ni, H.J., Wang, R.H., et al., 2017b. Comparative simulation research on the stress characteristics of supercritical carbon dioxide jets, nitrogen jets and water jets. Engin App Computational Fluid Mech 11 (1), 357–370. https://doi.org/10.1080/19942060.2017.1293565.

Li, M.K., Wang, G., Cheng, W.M., et al., 2021. Heat-fluid-solid coupling mechanism of supercritical carbon dioxide jet in rock-breaking. Petrol. Explor. Dev. 48 (6), 1450–1461. https://doi.org/10.1016/S1876-3804(21)60301.

Liao, H.L., Jia, X., Niu, J.L., et al., 2020. Flow structure and rock-breaking feature of the self-rotating nozzle for radial jet drilling. Pet. Sci. 17 (1), 211–221. https://doi.org/10.1007/s12182-019-00378-0.

Liu, B., Pan, Y., Ma, F., 2020. Pulse pressure loading and erosion pattern of cavitating jet. Engin App Computational Fluid Mech 14 (1), 136–150. https://doi.org/10.1080/19942060.2019.1695675.

Liu, S.Y., Li, H.S., Jiang, H.X., et al., 2023. Research progress and prospect of coal-rock breaking methods in mines. J. China Coal Soc. 48 (2), 1047–1069. https://doi.org/10.13225/j.cnki.jccs.2022.0733 (in Chinese).

Miroir, M., Laniel, R., Brient, A., et al., 2022. Water jet incremental sheet metal forming: a critical state-of-the-art review and a proposal for technological windows. Int. J. Adv. Des. Manuf. Technol. 119 (7), 4159–4175. https://doi.org/10.1007/s00170-021-08635-6.hal-03553007.

Ni, H.J., Wang, R.H., 2004. A theoretical study of rock drilling with a high pressure water jet. Pet. Sci. 11 (4), 72–76.

Nieto, F., Hargreaves, D.M., Owen, J.S., et al., 2015. On the applicability of 2D URANS and SST k - ω turbulence model to the fluid-structure interaction of rectangular cylinders. Engin App Computational Fluid Mech 9 (1), 157–173. https://doi.org/10.1080/19942060.2015.1004817.

Oh, T.M., Cho, G.C., 2014. Characterization of effective parameters in abrasive waterjet rock cutting. Rock Mech. Rock Eng. 47 (2), 745–756. https://doi.org/10.1007/s00603-013-0434-3.

Ozcelik, Y., Gursel, M., Ciccu, R., et al., 2012. Optimization of working parameters of water jet cutting in terms of depth and width of cut. Proc. Inst. Mech. Eng. Part E J. Process Mech. Eng. 226 (1), 64–78. https://doi.org/10.1177/0954408911407706.

Shen, H.L., Liu, Y., Wei, J.P., et al., 2023. Impact frequency variation of self-excited oscillation pulsed supercritical carbon dioxide jets. Petrol. Explor. Dev. 50 (5), 1097–1104. https://doi.org/10.1016/S1876-3804(23)60464-1.

Shen, Z., Sun, Q., 1988. Study of pressure attenuation of a submerged, nonfree jet and a method of calculation for bottomhole hydraulic parameters. SPE Drill. Eng. 3 (1), 69–76. https://doi.org/10.2118/14869-PA.
Srivastava, M., Nag, A., Chattopadhyaya, S., et al., 2021. Standoff distance in ultrasonic pulsating water jet. Materials 14 (88), 1–18. https://doi.org/10.3390/ma14010088.
Tian, C.L., Cheng, X.L., Wang, W., 2012. Experimental study on rock breaking with impacting water jet by modulation of chaos. Adv. Mater. Res. 535, 1751–1754. https://doi.org/10.4028/www.scientific.net/AMR.535-537.1751.
Wagner, W., Pruß, A., 2002. The IAPWS formulation 1995 for the thermodynamic properties of ordinary water substance for general and scientific use. J. Phys. Chem. Ref. Data 31 (2), 387–535. https://doi.org/10.1063/1.1461829.
Wang, F., Konietzky, H., Herbst, M., 2019. Influence of heterogeneity on thermo-mechanical behaviour of rocks. Comput. Geotech. 116, 103184. https://doi.org/10.1016/j.compgeo.2019.103184.
Wang, H.J., Liao, H.L., Wei, J., et al., 2023. Stress release mechanism of deep bottom hole rock by ultra-high- pressure water jet slotting. Pet. Sci. 20 (3), 1828–1842. https://doi.org/10.1016/j.petsci.2022.12.002.
Wang, H.Z., Li, G.S., Shen, Z.H., et al., 2015. Experiment on rock breaking with supercritical carbon dioxide jet. J. Petrol. Sci. Eng. 127, 305–310. https://doi.org/10.1016/j.petrol.2015.01.006.
Xiao, S., Ge, Z., Ren, Q., et al., 2020. Numerical analysis on the flow field structure and deflection characteristics of water jets under nozzle moving conditions. Engin App Computational Fluid Mech 14 (1), 1279–1301. https://doi.org/10.1080/19942060.2020.1822210.
Yang, R.Y., Li, G.S., Qin, X.Z., et al., 2022. Productivity enhancement in multilayered coalbed methane reservoirs by radial borehole fracturing. Pet. Sci. 19 (6), 2844–2866. https://doi.org/10.1016/j.petsci.2022.06.019.
Yar'Adua, K.H., John, I.J., Abbas, A.J., et al., 2021. An experimental study on high-pressure water jets for paraffin scale removal in partially blocked production tubings. J. Pet. Explor. Prod. Technol. 11 (2), 973–988. https://doi.org/10.1007/s13202-020-01009-w.
Yu, Z., Shao, J., Sun, Y., et al., 2023. Numerical analysis of hydro-thermal fracturing in saturated rocks by considering material anisotropy and micro-structural heterogeneity. Int. J. Rock Mech. Min. Sci. 170, 105457. https://doi.org/10.1016/j.ijrmms.2023.105457.
Zhang, J.L., Yang, F.W., Cao, Z.G., et al., 2023. Experimental study on ultra-high pressure water jet rock-breaking at high linear speed. Rock Soil Mech. 44 (3), 615–623. https://doi.org/10.16285/j.rsm.2022.0503 (in Chinese).
Zhang, P., Liu, Z., Yue, X., et al., 2022. Water jet impact damage mechanism and dynamic penetration energy absorption of 2A12 aluminum alloy. Vacuum 206, 111532. https://doi.org/10.1016/j.vacuum.2022.111532.
Zhao, J., Zhang, G., Xu, Y., et al., 2017. Mechanism and effect of jet parameters on particle water jet rock breaking. Powder Technol. 313, 231–244. https://doi.org/10.1016/j.powtec.2017.03.026.